Review of
Scientific Instruments

X-ray diffraction at the National Ignition Facility F

Cite as: Rev. Sci. Instrum. **91**, 043902 (2020); https://doi.org/10.1063/1.5129698
Submitted: 30 September 2019 . Accepted: 20 March 2020 . Published Online: 21 April 2020

J. R. Rygg, R. F. Smith, A. E. Lazicki, D. G. Braun, D. E. Fratanduono, R. G. Kraus, J. M. McNaney, D. C. Swift, C. E. Wehrenberg, F. Coppari, M. F. Ahmed, M. A. Barrios, K. J. M. Blobaum, G. W. Collins, A. L. Cook, P. Di Nicola, E. G. Dzenitis, S. Gonzales, B. F. Heidl, M. Hohenberger, A. House, N. Izumi, D. H. Kalantar, S. F. Khan, T. R. Kohut, C. Kumar, N. D. Masters, D. N. Polsin, S. P. Regan, C. A. Smith, R. M. Vignes, M. A. Wall, J. Ward, J. S. Wark, T. L. Zobrist, A. Arsenlis, and J. H. Eggert

COLLECTIONS

F This paper was selected as Featured

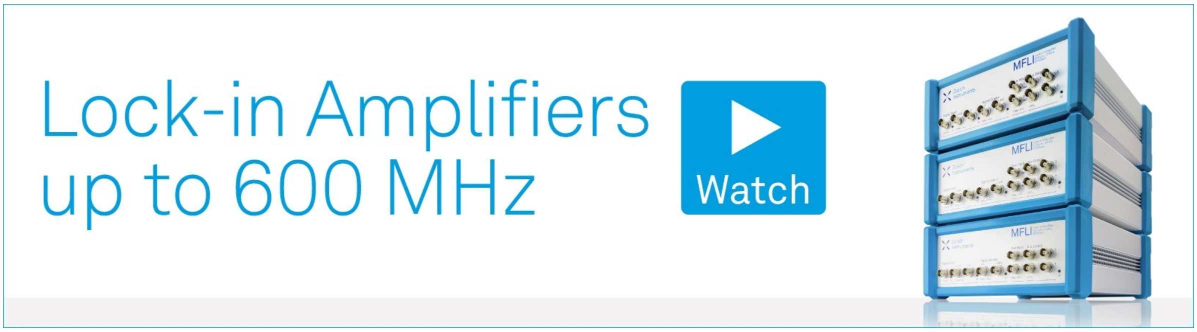

AIP Publishing

Review of
Scientific Instruments

ARTICLE

scitation.org/journal/rsi

X-ray diffraction at the National Ignition Facility

Cite as: Rev. Sci. Instrum. 91, 043902 (2020); doi: 10.1063/1.5129698
Submitted: 30 September 2019 • Accepted: 20 March 2020 •
Published Online: 21 April 2020

View Online Export Citation CrossMark

J. R. Rygg,[1,2,3,4,a)] R. F. Smith,[1] A. E. Lazicki,[1] D. G. Braun,[1] D. E. Fratanduono,[1] R. G. Kraus,[1] J. M. McNaney,[1] D. C. Swift,[1] C. E. Wehrenberg,[1] F. Coppari,[1] M. F. Ahmed,[1] M. A. Barrios,[1] K. J. M. Blobaum,[1] G. W. Collins,[1,2,3,4] A. L. Cook,[1] P. Di Nicola,[1] E. G. Dzenitis,[1] S. Gonzales,[1] B. F. Heidl,[1] M. Hohenberger,[1] A. House,[1] N. Izumi,[1] D. H. Kalantar,[1] S. F. Khan,[1] T. R. Kohut,[1] C. Kumar,[1] N. D. Masters,[1] D. N. Polsin,[2] S. P. Regan,[2] C. A. Smith,[1] R. M. Vignes,[1] M. A. Wall,[1] J. Ward,[1] J. S. Wark,[5] T. L. Zobrist,[1] A. Arsenlis,[1] and J. H. Eggert[1]

AFFILIATIONS

[1] Lawrence Livermore National Laboratory, Livermore, California 94551, USA
[2] Laboratory for Laser Energetics, University of Rochester, Rochester, New York 14623, USA
[3] Department of Mechanical Engineering, University of Rochester, Rochester, New York 14623, USA
[4] Department of Physics and Astronomy, University of Rochester, Rochester, New York 14623, USA
[5] Department of Physics, Clarendon Laboratory, University of Oxford, Parks Road, Oxford OX1 3PU, United Kingdom

[a)] **Author to whom correspondence should be addressed:** j.r.rygg@rochester.edu

ABSTRACT

We report details of an experimental platform implemented at the National Ignition Facility to obtain *in situ* powder diffraction data from solids dynamically compressed to extreme pressures. Thin samples are sandwiched between tamper layers and ramp compressed using a gradual increase in the drive-laser irradiance. Pressure history in the sample is determined using high-precision velocimetry measurements. Up to two independently timed pulses of x rays are produced at or near the time of peak pressure by laser illumination of thin metal foils. The quasi-monochromatic x-ray pulses have a mean wavelength selectable between 0.6 Å and 1.9 Å depending on the foil material. The diffracted signal is recorded on image plates with a typical 2θ x-ray scattering angle uncertainty of about 0.2° and resolution of about 1°. Analytic expressions are reported for systematic corrections to 2θ due to finite pinhole size and sample offset. A new variant of a nonlinear background subtraction algorithm is described, which has been used to observe diffraction lines at signal-to-background ratios as low as a few percent. Variations in system response over the detector area are compensated in order to obtain accurate line intensities; this system response calculation includes a new analytic approximation for image-plate sensitivity as a function of photon energy and incident angle. This experimental platform has been used up to 2 TPa (20 Mbar) to determine the crystal structure, measure the density, and evaluate the strain-induced texturing of a variety of compressed samples spanning periods 2–7 on the periodic table.

I. INTRODUCTION

At extreme pressures above a hundred gigapascal (100 GPa = 1 Mbar ≈ 1 × 10^6 atm), core electrons on neighboring atoms begin to interact, and matter has been observed to exhibit a variety of exotic behaviors. Examples include severe reduction in the melt temperature,[1,2] superionicity,[3,4] metals becoming transparent,[5] and insulators becoming conductors.[6–8] These dramatic changes in material properties under pressure have a number of practical consequences, including for the structure and evolution of astrophysical bodies and for various terrestrial applications such as inertial confinement fusion.

The response of matter at extreme pressures depends strongly on the particular structure or arrangement of the atoms. The structure of solids and liquids is a fundamental basis for understanding their mechanical, electronic, magnetic, and thermodynamic properties. Furthermore, first-principles theory increasingly predicts exotic and complex behavior under these conditions.[9–11]

The ability to study matter at extreme pressure and temperature conditions is often limited by the ability to create and maintain sufficient volumes of such materials at extreme conditions. Using laser-driven ramp compression at the National Ignition Facility (NIF), it is possible to reach pressures up to 5 TPa.[12,13] To probe the crystal structure of compressed materials at such extreme conditions, we have developed and implemented an *in situ* x-ray diffraction (XRD) platform at the NIF.

As with the diffraction platform demonstrated at the Omega Laser Facility,[14] a sample is sandwiched between tamper layers and compressed to a uniform, high-pressure state by direct laser drive of the assembly. The sample is then irradiated while at peak pressure by a burst of K-shell emission from separate laser-driven foils. The angular distribution of x rays scattered from a portion of the sample restricted by a pinhole aperture is recorded on x-ray-sensitive detectors covering approximately 1.5π sr.

This type of XRD platform has been used to observe new solid–solid phase transitions, the absence of expected phases, and the onset of melt.[4,15–21] Here, we report details of the implementation at the NIF (Sec. II), numerous refinements to the experimental setup (Sec. II) and analysis (Sec. III), and the evaluation of the system performance and uncertainties (Sec. IV).

II. EXPERIMENTAL SETUP

Two closely related variants of this experimental x-ray diffraction platform have been implemented: the Powder X-Ray Diffraction Image Plate (PXRDIP)[14] platform at OMEGA[22] and OMEGA EP,[23] and the TARget Diffraction *In Situ* (TARDIS) platform at the NIF.[24] Table I lists some basic capabilities of these facilities. Geometric restrictions allow only a subset of the facility beams to drive the sample package and x-ray source.

The primary components of the experimental setup (see Fig. 1) are the sample assembly, which includes a sample of the material being investigated; a foil target for the x-ray source; a pinhole aperture to restrict the detector field of view to the driven portion of the sample; and the diagnostic body, which holds the x-ray sensitive detector and also provides a clear line-of-sight for *in situ* determination of the pressure. These components are discussed in detail in Subsections II A–II E.

A. Sample assembly

The sample assembly (Fig. 2) is designed in concert with the drive-laser pulse shape (Sec. II D) to elevate and hold the sample of material under study at high pressure during x-ray exposure. The thin (3–50 μm) sample is sandwiched between two series of tamper layers that maintain the sample at a high and uniform pressure for several nanoseconds.

In its simplest configuration, the tampers consist of an ablator layer on one side and a window layer on the other. The laser pulse is incident on the front ablator layer, launching an increasing compression wave that propagates through the ablator and into the sample

TABLE I. Large laser systems with the x-ray diffraction (XRD) platforms described herein.

Facility	OMEGA	OMEGA EP	NIF
Total beams	60	4	192
Energy/beam (kJ)	0.5	5	9.4
Max pulse duration (ns)	3.5	10	30
XRD platform	PXRDIP	PXRDIP	TARDIS
Max sample drive beams	12	3	24
Max x-ray source beams	24	3	48

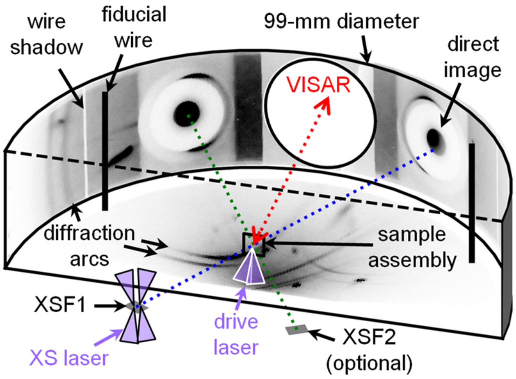

FIG. 1. The TARDIS experimental platform involves ramp compression of the sample assembly using temporally shaped NIF laser beams. One or optionally two x-ray source foils (XSFs) are driven by additional (XS) beams to generate an x-ray pulse which diffracts from the compressed sample and is recorded on image plates lining the inside of a 99-mm-diam cylinder. A hole in one image plate allows for simultaneous velocimetry of the sample assembly using the VISAR diagnostic in NIF port TC090-315. Shadows of tantalum fiducial wires inside the TARDIS body are used to cross-register the position and orientation of the image plates.

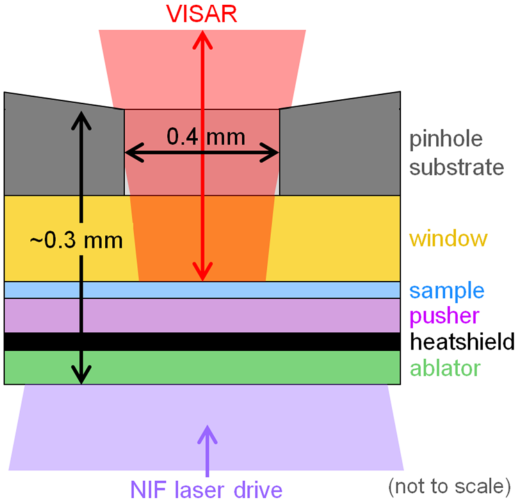

FIG. 2. The TARDIS sample assembly and pinhole. The laser drives compression by ablation of an ablator layer, transmitting the compression into the sample layer, sometimes through additional heat-shield and pusher layers. The pressure in the sample is maintained by a window tamper layer, through which the VISAR probe beam can track the package velocity.

and window. Velocity measurements of the system, either at the back free surface of a window that becomes opaque or at the sample–window interface for a window that remains transparent, are used to determine the pressure history in the sample, as described in detail in Sec. III F.

For some experiments, additional shielding is needed to reduce heating of the sample due to x rays from either the probe or the laser interaction with the ablator. In these cases, a heat-shield layer is inserted between the ablator and sample layers to absorb continuum x rays from the ablation plasma and/or the x-ray probe source. A separate pusher layer may be inserted between the heat shield and the sample either to improve the sequence of compression-wave reverberations within the sample assembly, or to reduce the thermal conduction of the heat shield into the sample, or for target fabrication limitations.

Table II lists the common materials and the range of typical thicknesses used for each layer.

Numerous considerations must be balanced when selecting materials for the tamper layers. First of all, the layers should not contribute a diffraction signal that can be confused with that from the sample. Various options include selecting an amorphous material, a material with very poor scattering efficiency (such as one with a low atomic number or low crystal symmetry), or by selecting a single crystal whose diffraction will be condensed into spots rather than the rings expected from a polycrystalline or "powder" sample.

Second, it is useful to consider the attenuation of the signal and background x rays of all layers due to their respective spectrally dependent optical depths. It is generally preferable to match the sample layer thickness to the optical depth of the probe x rays, as described in detail in Sec. IV A 3. Thicknesses of the remaining layers should be selected to factor in the signal-to-background and signal-to-noise ratios for the given x-ray load.

It is preferable that the ablator layer be made from a low-atomic-number material since that will increase the efficiency of ablation and result in lower background radiation at the same drive pressure. The heat shield, if used, should have a thickness that is matched to the x-ray load so as to maintain the sample in the solid state. A heat shield tuned to melt by the time of the x-ray probe will further avoid extraneous diffraction signals interfering with the data.

The response of the window to the pressure loading affects the determination of pressure within the sample, so it is critical to use a window material that has a well-characterized compression behavior. In addition, for transparent windows, the refractive-index variation with density must be known. Section III describes how pressure is determined in detail, and the uncertainty in pressure is discussed in Sec. IV E.

TABLE II. Layers in the sample assembly, common material choices, and range of typical thicknesses. The order is from the front "ablator drive" side to the back "diagnostic window" side. The heat-shield and pusher layers are sometimes omitted. C indicates the diamond polymorph of carbon, and CH refers to various plastics.

Layer	Materials used	Thickness range
Ablator	C, Be, and CH	20–200 μm
Heat shield	Au, Re, Ge, and Pb	2–15 μm
Pusher	C, CH, and Al	20–40 μm
Sample	Various	3–60 μm
Window	C, LiF, and MgO	40–200 μm

Finally, hydrodynamic impedance[25] mismatches between the layers result in reverberations as the compression waves encounter the various interfaces. If the impedance of the layers is matched, this eliminates reverberations and greatly simplifies the laser pulse shape design and reduces the uncertainty in the pressure history evaluation.

The layers in the sample assembly are typically affixed to each other using epoxy, which forms a low impedance layer at each interface. To minimize the effects of wave reverberations from the epoxy, it is preferable that this layer be very thin (<about 1 μm). In some cases, an epoxy bond can be eliminated by directly depositing one layer onto the neighboring part.

Additional <1 μm coatings are frequently applied to parts in the sample to modify the reflectivity of surfaces and interfaces in order to improve the quality of the data recorded by using the velocity interferometer (VISAR); see Sec. III F. To probe the motion of the interface between the window and a low-reflectivity sample, a 100–200 nm coating of a high-reflectivity metal such as Al or Ti is added to the side of the window facing the sample. For a high-reflectivity sample, a partial flash coating on the adjacent window allows VISAR to accurately measure both the time the wave leaves the sample and the time it enters the window, giving a measurement of the transit time through an epoxy layer at the interface. When the goal is to probe velocities of internal interfaces, it can be important to apply an appropriate antireflective coating at the window–vacuum interface for high-refractive-index windows. This reduces the intensity of light reflected from the stationary surface into the VISAR interferometer together with the reflected light from the moving interface, which would otherwise complicate the data analysis. Alternatively, when the motion of the free surface is desired, the antireflective coating is omitted and a thin metallic coating may be added.

For accurate hydrodynamic modeling of compression waves propagating through the sample assembly, it is important to know the individual component thicknesses to high accuracy. We use a double-sided non-contact ZYGO white-light interferometer to measure a 3-D thickness map of all parts before assembly and again during assembly after each subsequent epoxy layer is added, resulting in a thickness uncertainty of <0.2 μm for each component.

It is worth noting that *a priori* knowledge of the equation of state of the sample layer is not essential for determining the sample pressure since the equations of state of the tamper layers dominate the response of the package, particularly if the sample layer is thin. The sample will equilibrate with the immediately surrounding layers, even if there is an impedance mismatch, as long as the sample is thin enough so that the ramp duration occurs over several reverberation time scales.[6,8,14,26]

B. Pinhole

The sample assembly is directly mounted on a pinhole (i.e., a cylindrical aperture) in a high-atomic-number substrate, such as Pd, Ta, W, Re, Pt, or U-6Nb, to provide shielding to reject background x rays coming from the ablation plasma and to collimate the x-ray source (XS). Its diameter is chosen to contribute to the instrumental broadening approximately equal to the XS spatial extent and spectral bandwidth. Additionally, the pinhole is chosen to spatially filter the diagnostic field of view to the most spatially uniform region of the sample drive. The nominal pinhole diameter is 400 (300) μm for TARDIS (PXRDIP). In some cases, a larger diameter is used to increase the signal throughput, at a cost of a degradation of the instrument resolution and a reduction in the pressure uniformity of the exposed sample.

The diameter-to-thickness aspect ratio of the pinhole is a tradeoff between improved shielding (thicker substrate) and a larger solid angle of the detector with a line of sight to the sample. These experiments are commonly fielded with a pinhole aspect ratio of 4:1, allowing 1.5π solid angle, outside of which the detector is cut off by the critical exit angle of the aperture (at 76°, see Sec. IV A 4).

In some cases, x rays will diffract from the pinhole substrate at the edges. These ambient-pressure diffraction rings can be useful as a calibration reference for the 2θ scattering angle, provided they do not overlap with diffraction from the sample, which then complicates the analysis and interpretation.

In cases where it is not desirable to detect diffraction from the pinhole substrate, two mitigation strategies have been applied: first, the x-ray source wavelength can be chosen to be absorbed by the L-edge of the aperture substrate. This will severely reduce the volume contributing to diffraction, thereby reducing the signal, in many cases below the noise level. Alternatively, the substrate can be made from an amorphous material or a material with low crystal symmetry, such as U-6Nb. Both of these alternatives have been fielded to successfully eliminate the substrate diffraction, thereby allowing the maximum range of unobstructed 2θ space for the signal from the sample layer.

C. TARDIS hardware

The TARDIS hardware,[27,28] similar to that of PXRDIP,[14] includes mounting and positioning of the target, detector, and shielding in a combined assembly (Fig. 1). The combined assembly is constructed in two parts; the front target assembly and the back diagnostic assembly are joined with kinematic mounts and fasteners designed to withstand the transient loads delivered by up to several hundred kJ of laser energy. The final combined assembly is approximately 6 kg.

The target assembly holds the pinhole and sample assembly, provides a mount for the XS foil, and shields the interior image plates from high-energy x rays with a tantalum +10% tungsten (Ta10W) body.

Alignment pins are fixed to the body to facilitate orientation of the assembly and positioning of the pinhole in the NIF target chamber to within 50 μm accuracy. Additional alignment pins are located near the x-ray source foil to facilitate positioning of the alignment systems relative to the foil to ensure accurate alignment of the beams to the foil. The regions surrounding the target are covered by plastic-coated, dimpled shields, which angularly disperse specular reflections of unconverted 1ω and 2ω laser light to reduce their impact on laser optics.

The diagnostic assembly holds the detectors, fiducial wires, and various filters and shielding components. Three x-ray-sensitive image-plate (IP) detectors are arranged in the interior of the diagnostic assembly. One IP covers nearly half the inside of a cylinder of 49.5 mm radius, and two flat, nearly semicircular plates are placed on the top and bottom with 23.1 mm of separation. The IP's are held in position by magnets embedded in the walls of the diagnostic assembly body. Filters are placed in front of the image plates to reduce the x-ray background contribution from the XS and target drive plasmas.

Two vertical fiducial wires internal to the diagnostic assembly cast x-ray shadows on all three IP's, providing cross-registration of their positions and orientations with respect to the pinhole and the sample under study. The 0° (nonscattered) x rays from the XS that are transmitted through the target pinhole create a direct image on the curved back IP, which is also used in registering the experimental geometry. Fluorescence x-ray emission from this bright direct image is absorbed in the walls of a cylindrical Ta fluorescence shield to reduce the background on the IP's.

An aperture in the center of the back IP and surrounding diagnostic body allows access for the velocity interferometer (VISAR) probe beam.[29,30] The VISAR records the velocity of the target, which is used to determine sample pressure as a function of time, as described in Sec. III F. Debris from the sample assembly and pinhole that is accelerated by the NIF drive laser can be prevented from exiting the TARDIS box and contaminating the NIF chamber by placement of an optically transparent blast shield in the VISAR aperture.[28]

D. Laser setup

As with diffraction experiments at the Omega Laser Facility,[14] the desired thermodynamic state within the sample is generated with a temporally tailored laser pulse. This pulse ablates material from the surface of an ablator layer, creating the pressure wave that is transmitted into the sample itself.

Four quads (16 beams) on the NIF are typically used to drive the sample (Fig. 3). The quads are incident at 40°–46° from normal, with beam profiles smoothed using 1-mm continuous phase plates.[31,32] The beams are usually defocused and tiled in four quadrants to achieve a larger spot size and greater transverse pressure uniformity in the sample (see Sec. IV E 2 for more details). Alternatively, the beams can be overlapped into a smaller area to achieve the same drive pressure with less x-ray background at the cost of diminished drive planarity.

The sample is buried within the target between the ablator and a window, where the window acts to tamp the pressure in the sample for a long-enough duration for the x-ray diffraction measurement to be made. The laser pulse can be temporally shaped to

1. shock compress the sample, which concurrently raises the temperature and pressure to reach a Hugoniot state;[17]
2. shocklessly compress the sample from ambient, which results in nearly isentropic compression, with corrections due to dissipative effects in the sample (such as plastic work heating or phase transition kinetics) and external energy sources (such as x rays from the XS and ablation plasmas);[18–21] or
3. combine shocked and shockless compression to achieve a state intermediate between the isentrope and Hugoniot curves.[15,16]

Once the sample reaches the desired high-pressure state, a monochromatic x-ray beam, created by the He$_\alpha$ emission from a laser-irradiated foil and collimated by the pinhole supporting the

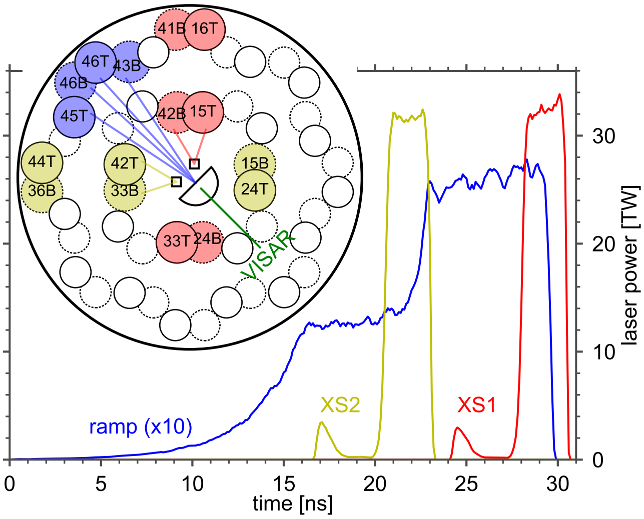

FIG. 3. Delivered laser power history designed to create two uniform pressure states at different times in a single drive. It shows an intermediate hold power on the way to peak power for the ramped sample assembly drive pulse (blue), with two x-ray source pulses (XS1 and XS2) timed to expose the sample at best uniformity at each of the associated pressures. Inset: assignment of NIF laser quads and schematic of pointing to the TARDIS sample assembly (blue) and to XS1 (red) and XS2 (yellow).

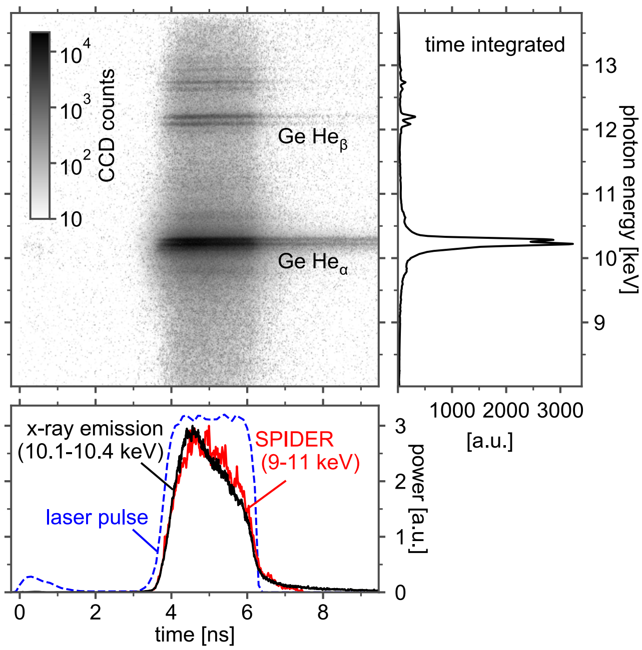

FIG. 4. Temporally resolved spectrum of x-ray source emission from a Ge foil driven with 28 kJ at 4 × 10^{15} W/cm^2 (NIF shot N141215-001) and recorded using the NXS diagnostic. The time-integrated spectrum shows that emission is dominated by Ge–He$_\alpha$ emission at 10.22 keV and 10.28 keV. A temporal lineout of the He$_\alpha$ complex (black curve) shows that x-ray emission is tightly correlated with the drive laser pulse (blue dashed curve) and is in close agreement with the independent x-ray emission history measured by SPIDER (red curve).

sample, is used as a source of photons for the *in situ* x-ray diffraction measurement, as described in detail in Sec. II E.

E. X-ray source

The x-ray source (XS) is generated through laser illumination of a metallic foil, ionizing the foil material to a helium-like state and inducing He$_\alpha$ (i.e., helium-like K-L$_{2,3}$) emission.[33,34] Temperature falls rapidly outside the laser spot incident on the foil, which restricts the spatial extent of the emission to be very close to the spot size (about 400 μm). In addition, the temperature falls rapidly when the driving laser is shut off, restricting the temporal extent of emission to the duration of the laser pulse (Fig. 4).

The x-ray source foil (XSF) is approximately 2 × 2 mm^2 at OMEGA or 3 × 4 mm^2 at the NIF, and 10–15 μm thick. Foil materials used previously include Fe, Ni, Cu, Zn, Ge, and Zr, with He$_\alpha$ wavelengths spanning the range from 1.9 Å to 0.8 Å. In some cases, the foil is deposited or glued to a 200-μm-thick layer of pyrolytic graphite, which improves the durability of the layer, and is required for otherwise too-brittle Ge.

The XSF is mounted directly on the TARDIS target assembly or positioned with a separate target positioner (PXRDIP) at a distance of 25–37 mm from the sample assembly and at a zenith angle of 29°–45° with respect to the pinhole axis. The XSF is illuminated by up to 136 kJ, 11 kJ, or 5 kJ of energy using up to 24, 22, or 3 beams at NIF, OMEGA-60, and OMEGA EP, respectively. The size of the beam spot on the foil is adjusted to balance high He$_\alpha$ yield and low detector background. The typical irradiance is between 1 × 10^{15} W/cm^2 and 5 × 10^{15} W/cm^2. Higher irradiance generally corresponds to foils with a higher atomic number.[34]

The laser energy is delivered to the XS foil in a flattop pulse between 0.5 ns and 2.0 ns long, depending on the desired tradeoff between signal and temporal resolution in the x-ray probe. In some cases, a lower-power picket about 4 ns before the main pulse is included (see Fig. 4), which preforms a plasma to increase the emitting mass during the main pulse, thereby increasing the conversion efficiency from laser energy to emitted He$_\alpha$ x-ray energy.[33]

Time-resolved spectra of XS emission are obtained at the NIF using the NXS diagnostic[35] (see Fig. 4). The spectrally integrated temporal emission history is also measured by SPIDER.[36] X-ray emission begins shortly after the rise of the main pulse and drops precipitously when the laser power is turned off. No He$_\alpha$ emission is observed during the prepulse.

X-ray emission in this energy range is dominated by the He$_\alpha$ complex. This result is confirmed by the time-integrated spectra obtained at the NIF using the Supersnout–II spectrometer[33] (Fig. 5) and at OMEGA with the Yaakobi x-ray spectrometer (XRS).[34,37,38] The intrinsic spacing between lines in the He$_\alpha$ complex $\Delta\lambda/\lambda$ is about 0.5% for the typical XSF materials (Ge = 0.6%).

The conversion efficiency for laser energy to x rays in the He$_\alpha$ complex is about 1%, with a contrast ratio compared to the x-ray continuum background of 50–100. K-shell satellite emission, in particular, the K$_\alpha$ and Ly$_\alpha$ lines, is a factor of 10 to 30 lower than the He$_\alpha$ emission. Transitions from higher orbitals, such as He$_\beta$, are also 10–100 times less intense than He$_\alpha$ and are further suppressed using

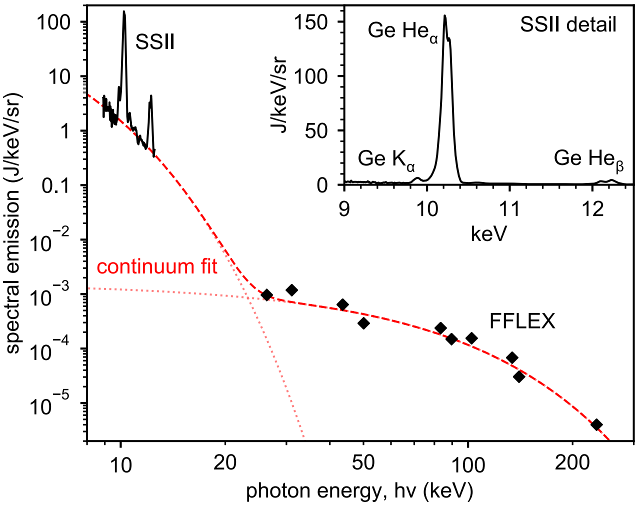

FIG. 5. Time-integrated x-ray source spectrum of NIF shot N140314-002 from a Ge foil driven at 3 × 10^{15} W/cm^2 with 26 kJ energy. Supersnout-II (SSII), channel 3 x-ray spectrum from 9 keV to 12.5 keV (solid curve) (inset: detail of the SSII spectrum), and ten FFLEX channels from 26 keV to 230 keV (diamonds). The x-ray continuum (excluding line emission) is well fit by a sum of two exponentials with slope constants of 1.8 keV and 38 keV (red dashed curve).

an appropriate K-edge filter in front of the detector—typically a thickness of approximately one optical depth of the x-ray source material at the He$_\alpha$ energy.

The continuum from the NIF x-ray source can be characterized by the sum of two exponentials: (1) a thermal component with about 8 × 10^{-3} of the incident laser energy and a slope constant $k_B T_1$ of about 1.8 keV and (2) a superthermal component with 3 × 10^{-5} of the incident energy and a slope constant $k_B T_2$ of about 38 keV (Fig. 5). The superthermal component is measured using the filter-fluorescer x-ray (FFLEX) diagnostic and originates from high-energy (100 keV) electrons produced through various laser–plasma instabilities.[39]

To irradiate the XS foil at the desired 1–5 × 10^{15} W/cm^2, the laser beams are overlapped and focused to a spot size of 250–500 μm on the foil, and the spatial extent of x-ray emission is approximately the same size (Fig. 6). Double-sided illumination of the foil is often used at OMEGA and the NIF, resulting in approximately twice the He$_\alpha$ yield with a minimal change in the size of the emitting region. A linear-beam-tiling arrangement is often used at the NIF where the foil is aligned edge-on to the aperture, and a series of spots are tiled in sequence on the foil along the vector to the aperture, creating a column source (Fig. 6). In this way, more energy can be deposited at a given irradiance without an increase in the apparent spot size when viewed from the pinhole.

At the NIF, we have also fielded two independently timed x-ray sources on the same experiment. Separate foils are positioned on opposite sides of the target assembly normal, approximately 60° apart (Fig. 1), with a laser configuration as shown in Fig. 3. The diffraction patterns from the two sources are easily distinguished based on their centers of curvature.

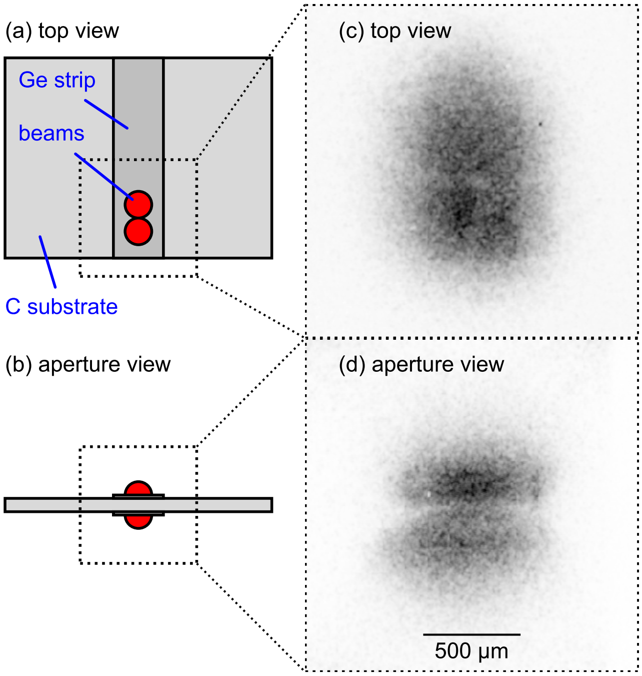

FIG. 6. (a) Top and (b) aperture (edge) views of a NIF x-ray source (XS) foil, with a 0.75 mm wide Ge strip on a 4 mm wide graphite substrate. Beams are linearly tiled near the edge closest to the pinhole (two beam spots shown, up to three spots used) and illuminate both sides of the XS foil. X-ray images as viewed from (c) above and (d) the location of the sample assembly and pinhole aperture with the same spatial scale. The aperture view shows the dual lobes of the top and bottom illumination spots. The total extent is about 0.5 mm wide and 0.7 mm high (FWHM) as seen from the pinhole aperture.

III. DATA PROCESSING

The primary results of the TARDIS and PXRDIP platforms are typically reported as a sequence of lattice d-spacings vs pressure. Reduction of the raw data to these results includes numerous processing steps, described in this section.

After exposure to the diffracted x rays, image plates (IP's) are protected from ambient light as they are transferred to an appropriate scanner, and the first scans are initiated between 25 min and up to several hours after the experimental shot. Scans produce a 2-D array of photostimulated luminescence (PSL) values, which can be mapped to incident photon fluence, as described in Sec. IV A 5. PSL values are corrected using the time delay between shot time and scan time.[40] Additional scans are performed if any pixel is saturated on the previous scan.

Corrections to the precise geometric arrangement of the x-ray source, pinhole, and image plates from their nominal values are determined using diffraction arcs and straight-through transmitted x rays, as described in Sec. III A. These geometric parameters enable one to project the IP scans into various traditional diffraction views, such as the stereographic and 2θ–ϕ projections, as described in Sec. III B. The geometric parameters are also used to evaluate corrections to the 2θ scattering angle on a per-pixel basis, as described in Sec. III C.

Many experiments have a slowly varying background, which is estimated and subtracted as specified in Sec. III D. Localized regions that are not diffraction from the pinhole or sample are identified and masked. The 2θ values of the individual x-ray diffraction lines are then determined through appropriate binning of the IP pixels, as described in Sec. III E. Lattice d-spacings are deduced by applying Bragg's law. Finally, the pattern of d-spacings is tested for consistency with proposed crystal structures, and mass density is inferred when a consistency is found.

The exact data processing workflow varies depending on details of the experiment, but for a typical shot, the analysis would proceed as follows:

1. mark features to fit on scanned image,
2. optimize geometric parameters,
3. estimate and subtract background,
4. verify features in stereographic or 2θ-ϕ projection,
5. mask regions with non-diffraction artifacts,
6. fit diffraction peaks for mean 2θ and intensity, and
7. infer crystal structure and density from peaks.

Again, for some experiments, better results may be obtained by altering the order listed above or by iterating. For example, if new diffraction lines are revealed after background subtraction, one would consider returning to step 1.

The pressure in the sample during x-ray exposure is deduced from the VISAR interferogram in a separate analysis, as described in Sec. III F.

A. Experimental geometry

The 2θ scattering angle corresponding to each pixel in the IP detector scans depends on the position and orientation of the IP's with respect to the pinhole and x-ray source (XS) at the time of exposure. The essential geometric arrangement for TARDIS is shown in Fig. 7.

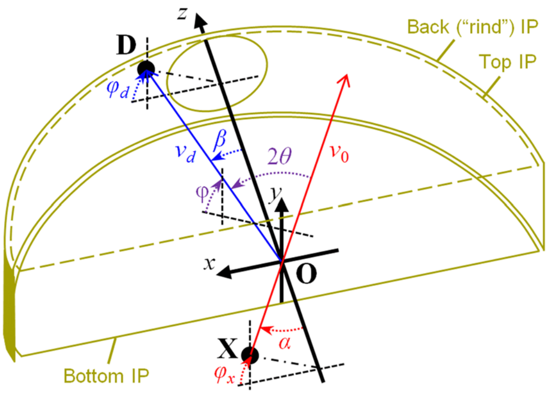

FIG. 7. The TARDIS experimental geometry. The coordinate system origin (**O**) corresponds to the pinhole center, with $\hat{z}$ toward VISAR, $\hat{y}$ "up" in the target chamber, and $\hat{x}$ completing the right-hand coordinate system. The sample assembly sits immediately on the $-z$ side of the pinhole substrate. X rays from an x-ray source (**X**) travel through **O** with vector $\vec{v}_0$. Some fraction of x rays are scattered by angle 2θ to a new vector $\vec{v}_d$, which encounters a detector element (**D**), on one of three image plates.

The experimental geometry is defined by two angular components for each x-ray source and three position and three orientation degrees of freedom for each IP; the origin is chosen to coincide with the center of the pinhole. PXRDIP has five IP's, and the standard TARDIS configuration has three IP's.

The nominal positions in the experimental setup are controlled to a few hundred micrometers by fabrication tolerance and target and diagnostic metrology. These constraints are sufficient to eliminate the two orientation degrees of freedom for each image plate that are "out of plane" of the IP; for TARDIS, this leaves only the yaw angle around the $\hat{y}$ axis for the top and bottom IP's and only the roll angle around the $\hat{z}$ axis for the back IP (see Fig. 7). For some TARDIS experiments, the y separation between the top and bottom plates is also constrained in the analysis. For other TARDIS experiments, the curved back IP is given two optional additional degrees of freedom corresponding to the radius of curvature and the azimuthal offset of the IP.

Analysis of 2θ using the nominal experimental geometry typically results in a precision of order 1° in 2θ. For improved 2θ precision, an optimization routine is run on the geometric parameters described above (between 10 and 18 parameters depending on the specifics) to find the best fit to the known or constrained 2θ values of features identified on the image plate scans.

Pixel locations of the fitting features are marked "by eye" and may include x-ray diffraction from the pinhole substrate, x-ray diffraction from the sample, the "direct" image of the x-ray source through the pinhole, or shadows of engineering features such as the fiducial wires in TARDIS. For dual x-ray source experiments, the direct images and diffraction lines must also track the originating x-ray source. In some cases, it is easier to mark the individual features after first background subtracting the IP scan, which is described below in Sec. III D.

Features of known 2θ include the direct image ($2\theta = 0$) and x-ray diffraction from the pinhole substrate (2θ = the value at the Bragg condition of the corresponding lattice plane at ambient density). In cases where the pinhole substrate does not give significant diffraction, diffraction lines from a compressed sample are used as input features for the optimization routine. In this case, the 2θ values are not known *a priori*, but points on the line are constrained to have the same 2θ along a given Debye–Scherer arc; this implicitly assumes that 2θ distortions along the arc due to pressure nonuniformity, strength in the sample, or finite grain size are small. All 2θ values are corrected for the systematic offsets described in Sec. III C.

The geometric optimization is constrained such that geometric parameters fall within the corresponding engineering tolerances. For TARDIS, additional optimization constraints are imposed by assuming the shadows of the fiducial wires are continuous across multiple IP's (see Fig. 8).

The effective 2θ precision resulting from the geometric optimization is typically 0.2°, described in more detail in Sec. IV C.

B. Geometric projections

With fitted values of the geometric parameters as described in Sec. III A, the spatial position and orientation of each detector pixel during the experiment are known. The detector surfaces can now be projected into arbitrary spaces, including many traditional x-ray diffraction coordinate systems.

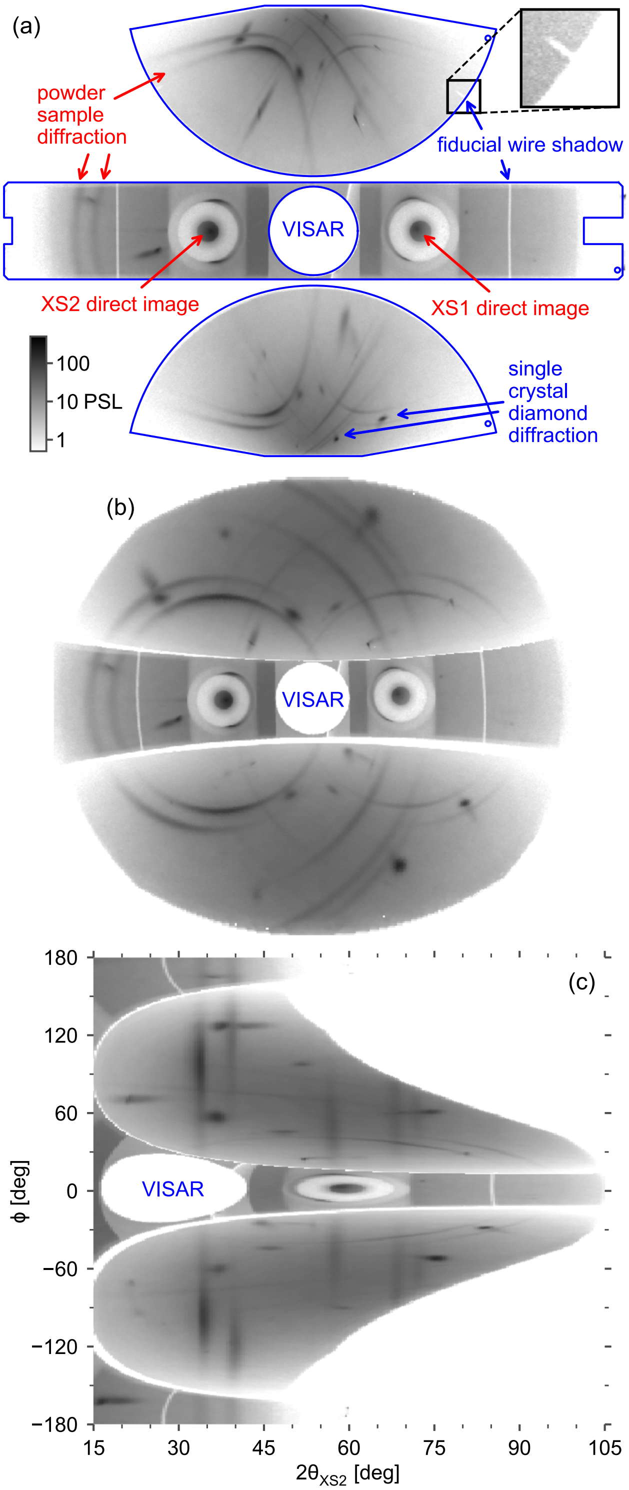

FIG. 8. Image plate scans for shot N160517-003 in $\log_{10}$(PSL) with no background subtraction and in three different projections: (a) flat (unprojected); (b) stereographic, centered on the VISAR access hole; and (c) 2θ–ϕ originating from x-ray source 2 (XS2).

One common x-ray diffraction projection is the stereographic projection, which when centered on the forward-scattered x rays results in circular Debye–Scherrer rings. This projection is also useful for assessing non-diffraction features in the data, such as shadows of the fiducial wires. For dual x-ray source experiments, stereographic projection centered on the $\hat{z}$/VISAR/drive normal axis (rather than an x-ray source direct image axis, ν_0) puts the two diffraction patterns on an equal footing [see Fig. 8(b)].

The 2θ–ϕ projection [Fig. 8(c)] allows us to assess the azimuthal dependence of the diffractogram, where 2θ is the x-ray scattering angle and ϕ is the azimuthal angle around the direct transmitted beam. The scattering angle 2θ can be calculated to each detector pixel by considering the zenith angle between the transmitted beam vector $\vec{v}_0$ and the vector to an individual detector pixel, $\vec{v}_d$,

$$\cos 2\theta = \vec{v}_0 \cdot \vec{v}_d. \tag{1}$$

The azimuthal angles can be similarly calculated, where we have chosen $\phi = 0$ to correspond to the direction defined by the unit-normal to the sample assembly, $\hat{z}$ (also coincident with the axis of the cylindrical pinhole aperture),

$$\cos\phi = (\vec{v}_0 \times \vec{v}_d) \cdot (\vec{v}_0 \times \hat{z}). \tag{2}$$

Note that the azimuthal angle ϕ of the diffracted beam is with respect to the scattering angle 2θ compared to the $\vec{v}_0$ axis, whereas the azimuthal angles ϕ_x and ϕ_d of the x-ray source and detector pixel are with respect to the α and β zenith angles compared to the VISAR or z axis.

Two other projections are sometimes used for specific analyses of the dynamically compressed samples. The 2θ–χ projection can be helpful for assessing off-diagonal components of any deviatoric strain of the sample. Here, χ is the angle between the scattering plane normal and the compression axis,

$$\cos\chi = (\vec{v}_0 - \vec{v}_d) \cdot \hat{z}. \tag{3}$$

The standard TARDIS geometry is not optimized to cover a large range of χ. The 30° angle between $\hat{z}$ and $\vec{v}_0$, and 1:4 pinhole aspect ratio limits the χ range between 70° and 140°.

Characterization of the spatial extent of compression is often done in the 2θ–β projection, where β is the zenith angle of the pixel with respect to the sample normal,

$$\cos\beta = \vec{v}_d \cdot \hat{z}. \tag{4}$$

The spatial extent of the sample compression is influenced by edge rarefactions due to the finite extent of the drive beams; the resulting transverse variation in uniformity is discussed further in Sec. IV E 2.

C. Determination of scattering angle 2θ

Optimization of the system geometry, as described in Sec. III A, yields geometric parameters that can be used to precisely determine the nominal scattering angle $2\theta_n$ from each x-ray source **X** to every detector pixel **D** through the origin at the pinhole center **O**. However, by design, there is no material at point **O** to scatter anything; scattering occurs within the sample layer or pinhole substrate that are displaced from **O** by a small but non-negligible offset.

These offsets lead to a systematic difference from the nominal scattering angle, of order 0.5° for our typical setup. Integrals to calculate these corrections are presented in this section, with evaluation of the integrals in Secs. III C 1 and III C 2.

We again choose as the origin **O** the center of the cylindrical aperture in the pinhole substrate, where the z axis coincides with the pinhole axis, and **D** is on the $+z$ side of the aperture. The spherical coordinates of each **X** and **D** in this coordinate system are given by $(r_x, \pi - \alpha, \phi_x)$ and (r_d, β, ϕ_d), respectively (see Fig. 9).

The nominal scattering angle, $2\theta_n$, is calculated as $\pi - \angle XOD$, which can be expressed as

$$\cos 2\theta_n = \cos\alpha\cos\beta - \sin\alpha\sin\beta\cos(\phi_d - \phi_x). \tag{5}$$

Figure 9 shows a sketch of the situation at $\phi_d = \phi_x$; for this special case, $2\theta_n = \alpha + \beta$.

X rays are scattered in the sample assembly (e.g., at point **S**) or within the pinhole substrate (e.g., at point **P**), see Fig. 9. The location of these scattering sites is offset from the origin **O**, typically by a distance that is small compared to r_x and r_d, but not negligible—of order 1%. The precise value of this offset depends on the position of the scattering site as well as the positions of **X** and **D**.

For the kth scattering volume of total volume V_k, the average scattering angle is

$$2\theta_{k,\text{ave}} = \frac{1}{V_{k0}}\int_{V_k} 2\theta_k(\vec{r})T(\vec{r})d^3\vec{r}, \tag{6}$$

where the effective volume V_{k0} is

$$V_{k0} = \int_{V_k} T(\vec{r})\mathrm{d}^3\vec{r}. \tag{7}$$

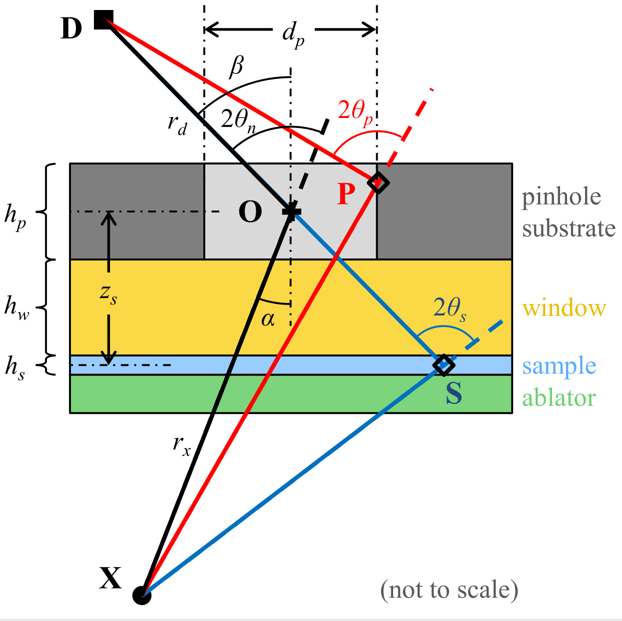

FIG. 9. X rays originating from the x-ray source **X** and detected by a detector pixel **D** will undergo a slightly different scattering angle when scattering off the sample **S** or pinhole substrate **P** compared to a nominal angle calculated at the center of the pinhole, **O**. The azimuthal angles ϕ_x and ϕ_d of points **X** and **D**, respectively, are measured in a right-hand coordinate system around the pinhole axis (see Fig. 7).

A scattering volume that has uniform density and structure factor and an unobstructed line of sight to both **X** and **D** will have a weighting function at a point **K** equal to the net transmission $T_k = e^{-\mu_k s}$. Here, μ_k is the linear attenuation coefficient in material k and s is the total distance traversed in the material along the path XKD.

Subsections III C 1 and III C 2 discuss the setup and evaluation of the integral of Eq. (6) for diffraction from the sample layer and the pinhole substrate.

1. *Systematic correction to sample 2θ*

The volume of the sample seen by the detector element **D** is restricted to a cross-sectional area that has an unobstructed view through the pinhole, described in Sec. IV A 4. The middle of the sample layer is displaced with respect to the origin **O** by a distance $z_s = h_w + (h_p + h_s)/2$ in the $-z$ direction (Fig. 9), where h_w, h_p, and h_s are the thicknesses of the window, pinhole substrate, and sample, respectively. At the time of x-ray exposure, this displacement will be diminished compared to its starting value due to motion and compression of the sample and window during the drive. The velocity in the sample assembly is directly observed by the VISAR, and the value of z_s and the thickness h_s at the time of x-ray exposure are calculated precisely through integration of the VISAR record. Using the linear attenuation coefficient μ_s of signal x rays in the sample, the evaluation of Eq. (6) is used to determine the average scattering angle in the sample, $2\theta_s$.

A convenient approximation, accurate to first order in z_s/r_x, is that the average scattering angle for the exposed sample is equal to the scattering angle for a point in the middle of the sample layer at z_s and along a vector colinear with **O** and **D**, as shown by point **S** in Fig. 9. The spherical coordinates of point **S** are $(z_s \sec\beta, \pi - \beta, \pi - \phi_d)$. **S** is always coplanar with points **X**, **O**, and **D**, and the sample correction to the nominal scattering angle is

$$\tan(2\theta_s - 2\theta_n) = \frac{\sin(2\theta_n)}{(r_x/z_s)\cos\beta - \cos(2\theta_n)}. \tag{8}$$

For the standard TARDIS geometry, this first-order correction to the sample scattering angle, $2\theta_s - 2\theta_n$, is of order 0.5°, as shown in Fig. 10. The corresponding second-order correction has magnitude $(d_p/r_x)^2$, not more than 0.01°, and is neglected.

2. *Systematic correction to pinhole 2θ*

Although some experiments are set up purposefully to reduce or eliminate the diffraction signal from the pinhole substrate, in other cases, diffraction at known scattering angles from the ambient-density pinhole substrate is used to calibrate the system geometry for a more-accurate map of 2θ across the detector. The physical space occupied by the pinhole substrate is slightly displaced from the sample and results in a systematic correction to 2θ that is different from that for the sample (see Fig. 9).

We consider a right-cylindrical aperture of diameter d_p in an absorbing substrate of thickness h_p and linear attenuation coefficient

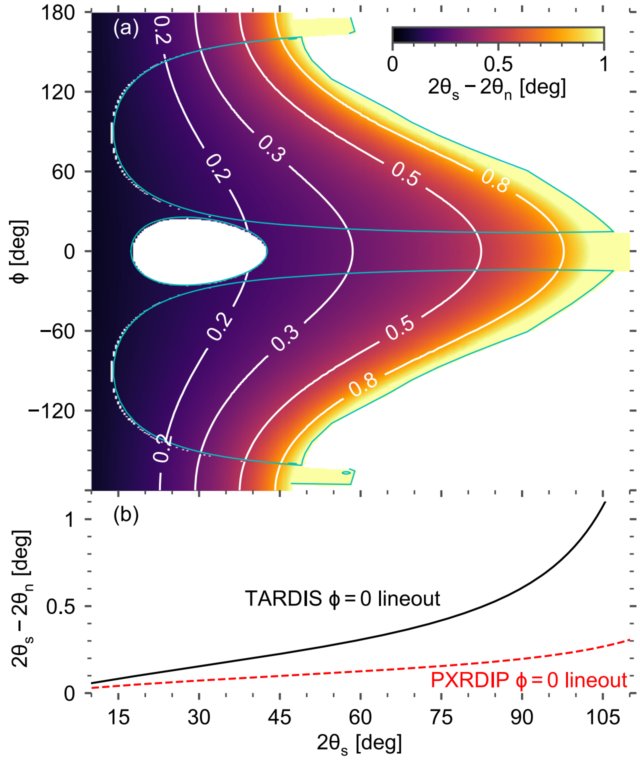

FIG. 10. (a) Magnitude of the sample 2θ correction, $2\theta_s - 2\theta_n$, arising due to the finite displacement of the sample from the pinhole center, as depicted in Fig. 9. The magnitude of the correction scales approximately linearly with the sample offset and is typically less than 1°. (b) The $2\theta_s - 2\theta_n$ correction at $\phi = 0$ (when incident and scattering vectors are coplanar with the z axis) for nominal TARDIS (black solid curve) and PXRDIP (red dashed curve) geometries. The larger magnitude for TARDIS arises primarily due to the thicker nominal window used with the longer compression pulse length.

μ_p. The origin **O** is at the center of the cylinder, with the cylinder axis aligned along the z axis and the x-ray source **X** on the $-z$ side of the substrate. An element of the pinhole substrate **P** is at the cylindrical coordinates $(d_p/2, \phi_i, z_i)$, where $z_i \in [-h_p/2, h_p/2]$. Assuming an optically thick pinhole ($\mu_p h_p \gg 1$), we consider only substrate elements corresponding to the cylinder's surface as contributing to the detected scattering.

For the pinhole volume, the integral in Eq. (6) can be evaluated using a number of methods. Here, we derive an analytic approximation accurate to first order in $\{h_p, d_p\}/\{r_x, r_d\}$, which expedites the computation of the pinhole systematic 2θ correction, especially useful for optimization of the geometric fit described above. The three main components of the integral are the scattering angle $2\theta_i$ from each pinhole element, the integration limits over the surface of the pinhole, and the weighting function.

The scattering angle $2\theta_i$ from any pinhole element to any detector element is $\pi - \angle\mathbf{XPD}$ and is not, in general, equal to $2\theta_n$. This angle can be calculated by shifting the origin from **O** to **P**, recalculating the spherical coordinates in the shifted coordinate system and computing the scattering angle as in Eq. (5),

$$\cos 2\theta_i = \cos\alpha_i \cos\beta_i - \sin\alpha_i \sin\beta_i \cos(\phi_{di} - \phi_{xi}), \tag{9}$$

where subscript i indicates angles in this shifted coordinate system. In terms of the nominal angles, the shifted angles are

$$\tan\alpha_i = \frac{\sqrt{\sin^2\alpha - 2b_x \sin\alpha\cos(\phi_x - \phi_i) + b_x^2}}{\cos\alpha + z_i/r_x}, \tag{10}$$

$$\tan\beta_i = \frac{\sqrt{\sin^2\beta - 2b_d \sin\beta\cos(\phi_d - \phi_i) + b_d^2}}{\cos\beta - z_i/r_d}, \tag{11}$$

$$\tan\phi_{xi} = \frac{\sin\phi_x - b_x\sin\phi_i}{\cos\phi_x - b_x\cos\phi_i}, \tag{12}$$

$$\tan\phi_{di} = \frac{\sin\phi_d - b_d\sin\phi_i}{\cos\phi_d - b_d\cos\phi_i}, \tag{13}$$

where $b_x = d_p/2r_x$ and $b_d = d_p/2r_d$.

The integration limits do not need to encompass the entire surface of the pinhole; the near edge of the substrate will occlude part of the surface from illumination by the x-ray source at **X** and from direct vision by the detector element **D**, depending on their relative positions. The z_{xi} and z_{di} curves defining the boundary of illumination by **X** and direct vision by **D**, respectively, are

$$z_{xi} = -h_p/2 + d_p \cot\alpha \cos(\phi_x - \phi_i + \pi), \tag{14}$$

$$z_{di} = h_p/2 - d_p \cot\beta \cos(\phi_d - \phi_i + \pi), \tag{15}$$

where we have approximated the zenith and azimuthal angles of **X** and **D** by their nominal values across the surface, which is accurate to first order in $\{h_p, d_p\}/\{r_x, r_d\}$.

Note that even if β is larger than the critical angle of the pinhole, $\tan\beta_{crit} = d_p/h_p$, the areas bounded by these curves can still intersect, resulting in a scattered signal from the pinhole in a detector region that is "blind" to scattering from the sample. Note also that these curves do not intersect on the surface of the pinhole for $\cos(\phi_d - \phi_x)$ in the vicinity of -1; these areas on the detector can nonetheless see scattering from the pinhole substrate that either enters the front or exits the back of the substrate near the edges.

To handle these different x-ray entrance and exit scenarios, the volume integral of Eq. (6) is split into a piecewise consideration of three cases (see Fig. 11): (1) entrance and exit from the inner surface of the pinhole, (2) entrance in the inner surface and exit from the back face, and (3) entrance in the front face and exit from the inner surface,

$$V_0 = V_1 + V_2 + V_3. \tag{16}$$

A fourth case, where x rays enter the front face and exit the back face, is neglected in our limit of an optically thick pinhole substrate, $\mu_p h_p \gg 1$. More-complex paths of multiple entrances and exits are also neglected.

For case 1, the contribution from the pinhole inner surface, we approximate the surface locally as a plane, where x rays are incident at angle ψ_x and exit at angle ψ_d with respect to the surface normal. To first order, these angles can be related to the coordinates of

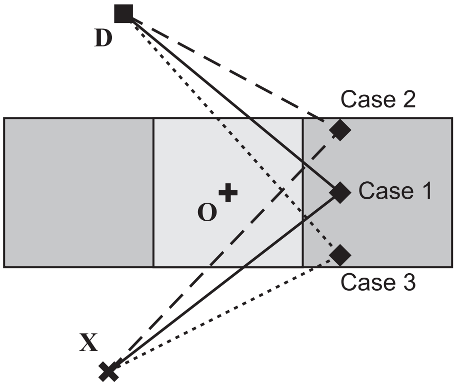

FIG. 11. Calculation of the pinhole 2θ scattering correction is separated into three cases: (1) entrance and exit from the pinhole inner surface, (2) entrance in the inner surface and exit from the back (D-side) surface, and (3) entrance in the front (X-side) surface and exit from the inner surface.

P, **X**, and **D**: $\cos\psi_x = \sin\alpha\cos(\pi + \phi - \phi_x)$ and $\cos\psi_d = \sin\beta\cos(\pi + \phi - \phi_d)$. Integrating over depth into the substrate x, and neglecting the small differences in 2θ over depth, we obtain the effective volume per unit surface area,

$$\frac{\mathrm{d}V_1}{\mathrm{d}A} = \frac{1}{\mu_p(\sec\psi_x + \sec\psi_d)}. \tag{17}$$

The effective volume for case 1 is then reduced to

$$V_1 = \frac{d_p}{2}\int_{z_1}^{z_2}\int_{\phi_1(z)}^{\phi_2(z)}\frac{\mathrm{d}V_1}{\mathrm{d}A}\,\mathrm{d}\phi\mathrm{d}z, \tag{18}$$

where the limits in z and ϕ cover the region of the surface with a direct line of sight to both **X** and **D**.

For case 2, the contribution from the **D**-side edge, we again have x rays incident on the inner surface at angle ψ_x, but now they exit from the back face at angle β. Integrating along the radial and axial directions, and neglecting the small differences in 2θ over this area, we obtain the effective volume per unit length along the perimeter,

$$\frac{\mathrm{d}V_2}{\mathrm{d}l} = \frac{1}{\mu_p^2\sec\psi_x(\sec\beta + \sec\psi_x\tan\eta_d)}, \tag{19}$$

where $\tan\eta_d = \cos\beta\cos(\phi - \phi_d)$ if $\cos(\phi - \phi_d) > 0$ and 0 otherwise. The effective volume for case 2 is then

$$V_2 = \frac{d_p}{2}\int_{\phi_1}^{\phi_2}\frac{dV_2}{dl}\mathrm{d}\phi. \tag{20}$$

The integration limits are $\phi_{1,2} = \pi + \phi_x \pm \arccos(\frac{h_p}{d_p}\tan\alpha)$ if $\alpha < \beta_{crit}$; otherwise, the integral is zero (**D**-side edge is not illuminated by the x-ray source).

Case 3 is identical to case 2 but with the roles of **X** and **D** swapped, along with their associated distances and angles.

The differences of pinhole-averaged and sample-averaged 2θ compared to nominal $2\theta_p - 2\theta_n$ and $2\theta_s - 2\theta_p$, respectively, are shown in Fig. 12.

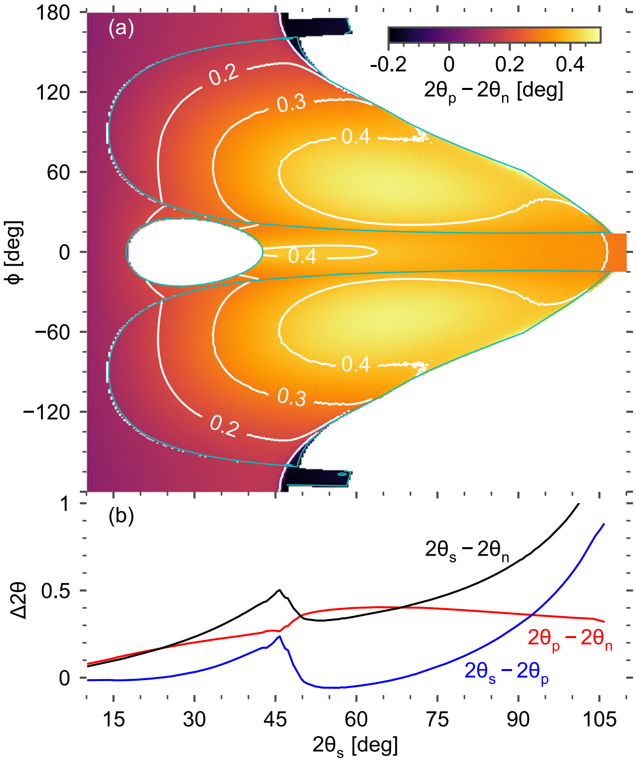

FIG. 12. (a) The magnitude of the pinhole 2θ correction compared to nominal $2\theta_p - 2\theta_n$, as depicted in Fig. 9 for nominal TARDIS geometry. (b) Differences between $2\theta_s$, $2\theta_p$, and $2\theta_n$, azimuthally averaged over the detector region with a view of the sample ($\beta < \beta_{crit}$).

D. Background subtraction

The background on the detectors originates from two plasma regions with distinct spatial, spectral, and temporal characteristics: the region formed by laser illumination of the x-ray source foil and the region formed by laser ablation of the sample assembly. However, since the current detectors (image plates) are time integrating, we will ignore the temporal differences for this discussion.

The XSF is typically irradiated at 10^{15}–10^{16} W/cm^2 in order to achieve temperatures high enough for efficient He$_\alpha$ emission of the foil material. This is above the threshold for many laser–plasma instabilities;[41] as a result, there is substantial hot-electron production and ensuing hard x-ray generation with a characteristic exponential spectrum with slope constant near 40 keV. Although the detectors are shielded from direct exposure to this background, some fraction is able to "punch through" the shielding, especially in the vicinity of the target, some of which induces fluorescence of the shielding, the aperture substrate, and the detector itself, resulting in a broad, hard x-ray background.

The sample assembly is typically irradiated at 10^{13}–10^{14} W/cm^2 in order to produce ablation pressures of 0.1–2 TPa. This results in a substantially cooler plasma than that produced by the XSF illumination, resulting in a softer x-ray spectrum. However, this plasma region sits just outside the aperture, so the effectiveness of line-of-sight shielding is greatly diminished.

The relative contributions of these sources to each other and to the signal depend on details of the laser pulse shape and total energy; signal-to-background (S/B) ratios from 1 to 10 are typically observed for sample pressures below 0.3 TPa, but S/B of 0.1 or less is not uncommon at pressures of 1–2 TPa. Fortunately, the spatial characteristics of the signal and the background are distinct: signal lines tend to follow contours of constant 2θ with a width characteristic of the instrumental broadening ($\approx 1^\circ$ FWHM), whereas the background has a more extended character. One can take advantage of this difference with appropriate digital filtering methods.

The Gaussian bandpass or difference-of-Gaussians method used previously[14] is closely related to the Laplacian-of-Gaussian method. This strategy highlights image regions with large curvature, such as at the peaks of the signal lines. It is sufficient for determining the positions of the signal lines, but drawbacks include the generation of oscillations near the sharp lines and modification of the amplitude of the signal, both of which complicate the analysis.

Here, we describe a variant of the Statistics-sensitive Non-linear Iterative Peak-clipping (SNIP) algorithm to estimate and subtract the background.[42–44] A coarse outline of the algorithm follows.

Starting with an array of detector values, D, we first normalize D such that a value of 1 corresponds to the expected value for one signal photon. For the image plates used here, $N = D/Q$, where $Q \approx 6 \times 10^{-3}$ PSL/photon, and is expressed more precisely in Sec. IV A 5. We then apply the log-log-square root (LLS) operator,

$$X_0 = \log\{\log[\sqrt{N+1}+1]+1\}, \tag{21}$$

where the square root selectively enhances small peaks and the repeated logarithms compress the dynamic range of the normalized signal.

The background is then successively estimated through an iterative comparison loop with an incrementing window size. If we consider the 1-D case, the pth iteration of the background at point i, $X_p(i)$, is calculated from the previous $(p-1)$ iteration as the minimum of $X_{p-1}(i)$ and the average of the values at a distance p away,

$$\begin{aligned} a_p(i) &= X_{p-1}(i),\\ b_p(i) &= [X_{p-1}(i+p)+X_{p-1}(i-p)]/2,\\ X_p(i) &= \min[a_p(i), b_p(i)]. \end{aligned} \tag{22}$$

The iteration is continued up to some maximum window size w. The net effect of this procedure is for the background estimation to hug troughs and clip peaks that are narrower than w.

After the iteration procedure mentioned above, the dynamic range is re-expanded with the inverse of the LLS operator,

$$B = Q(\{\exp[\exp(X_w-1)-1]\}^2-1), \tag{23}$$

where B is the background estimate in the original detector (D) units. The estimate of the true signal S is obtained by subtracting B from the original detector signal D.

A number of refinements to this procedure are implemented, some of which were described previously,[43,44] including a fourth-order clipping filter, a decrementing window size, simultaneous smoothing for reduction of noise artifacts, and generalization to multidimensional data.

The 2-D version as described by Morháč *et al.*[43,44] was designed to eliminate background ridges to find coincidence peaks in gamma-ray spectra. In our case, the signal has the character of relatively narrow ridges on a broader background. Furthermore, these signal ridges are not, in general, horizontal or vertical or even "straight" in the detector coordinate system but rather follow contours of constant 2θ.

We can address this issue in a couple different ways. For example, to take advantage of the known 2θ path of the signal ridges, we can first project the data images into $2\theta - \phi$ space, as described above, and then perform a 1D SNIP procedure at each ϕ along the 2θ direction or optionally with some azimuthal smoothing. In such cases, we choose the filter window w to be twice the expected instrumental FWHM broadening in 2θ. Care must be taken, however, if there are closely spaced peaks (spacing < FWHM), in which case the window should be broadened accordingly to avoid "filling in" the nearby peaks.

The abovementioned method does an excellent job of selecting ridges along the expected 2θ direction, drastically reducing ridges with other orientations. However, in some cases, we may wish to view ridges at all orientations, and not preferentially select a particular orientation, such as data with dual x-ray source exposure. In such cases, we apply the 2-D SNIP algorithm to the original data images but with an isotropic filter kernel chosen for rotational symmetry.

An example of the results from this background subtraction algorithm is shown in Fig. 13. This method has been used to identify and locate the positions of peaks with signal to background ratios (S/B) down to about 1%.

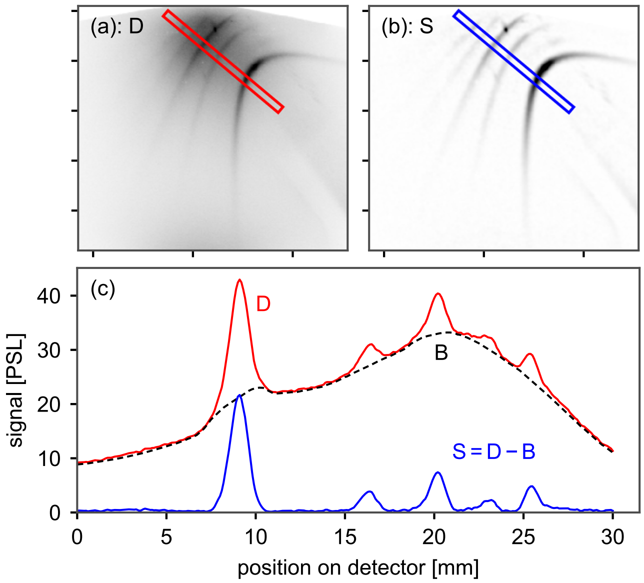

FIG. 13. (a) Original scan D and (b) background-subtracted signal $S = D - B$ of the top image plate from shot N140908-001. (c) The first five lines from bcc Pb at 200 GPa are evident in the image lineouts. The modified-SNIP background estimate has been used to locate line positions on this platform with S/B down to nearly 1%.

E. Line fitting

Lineouts of the image data are generated from the original pixels, with either the original image D, the background-subtracted signal S, or the normalized signal R. To obtain the normalized signal, S is divided by the pixel-wise determination of the instrument response function G, as described in Sec. IV A 6. It should be noted that the instrument response is calculated at the wavelength of the signal photons, but the background, in general, will have a broader spectrum. The normalization, therefore, distorts the true signal-to-background intensity ratio, and so, the normalization step is generally applied after background subtraction to minimize this effect.

In addition to spatially broad background radiation arising from the ablation plasma radiation, broadband radiation from the XS, and various fluorescence sources, we also observe spatially localized background features. These features can arise from the shadows of engineering features or by highly textured diffraction from the ablator, pusher, heat shield, window, and pinhole substrate components. Similar features may also arise from single-crystal Laue diffraction due to the spectrally broad XS background radiation. This broadband Laue diffraction can be used to supplement the geometric fitting procedure discussed above but also contributes unwelcome distortions to the diffractogram. Such artifacts are, therefore, masked and excluded before generating the diffractogram by binning pixels as a function of 2θ (see Fig. 14).

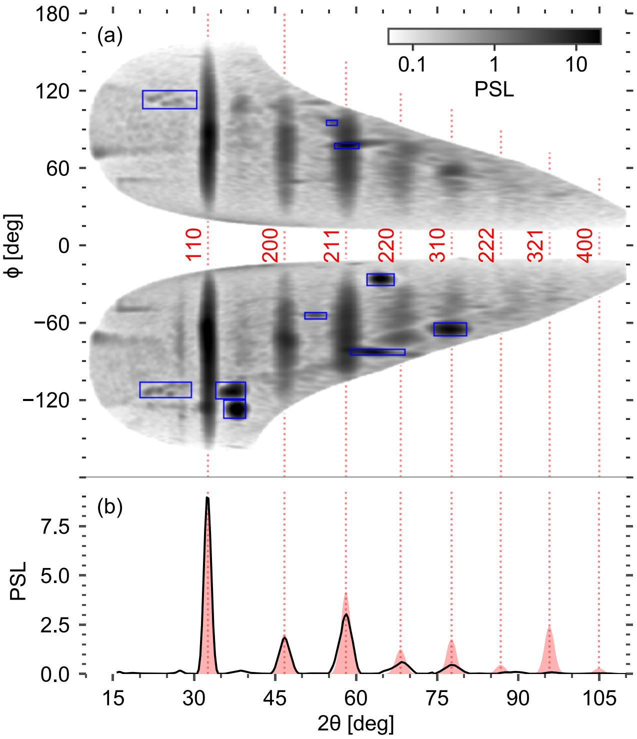

FIG. 14. (a) Background-subtracted signal S on the top and bottom plates of shot N140908-001 (Ge XS exposure of a Pb sample at 200 GPa) in the 2θ–ϕ projection. (b) The azimuthally averaged lineout (black) is compared to diffraction expected from a body-centered-cubic lattice with constant a = 3.05 Å (shaded red); Miller indices of the corresponding lattice planes are also indicated. Blue rectangles in (a) indicate regions which contain spurious or real signals that are not from the sample of interest, including diffraction spots from the compressed diamond window. Data within these regions are excluded from the lineout shown in (b).

Locations of Bragg peaks in the resulting diffractogram are identified either manually by the user or algorithmically based on peak amplitude or signal-to-noise criteria. The region surrounding and including the line is fit with a Gaussian, optionally including low-order polynomial terms, to approximate any residual background. Closely spaced peaks are fit with multiple Gaussians on a single background polynomial. The result is a sequence of Bragg-peak scattering angles, linewidths, and integrated intensities.

The Bragg-peak information is then compared to various candidate crystal structures. If there are only a few lines and more than one candidate structure produces a good match, then density arguments may be invoked to eliminate the candidates from consideration.

F. Pressure determination

The pressure in the sample at the time of x-ray exposure is determined through analysis of the VISAR velocity record.[29,30] The NIF dual-channel line-imaging VISAR measures velocity history by detecting Doppler shifts of a 660-nm optical probe reflecting off a moving surface in the target (i.e., the sample–window interface through a transparent window, a reflecting shock front, or the free surface). The reflected image is passed through a Mach–Zehnder interferometer containing a dispersive etalon in one leg, encoding the probe Doppler shift in the phase of the resulting fringes. Time-resolved velocity is extracted from the interferogram images as described previously.[29,45]

In addition to the measured velocity, sample pressure history depends on the compression path (e.g., shock,[17] multishock,[15,16] or ramp[18–20]), the target constituents (Fig. 15), the wave interactions with the target components, and the strength of the sample and tamper materials. Several methods are available for the determination of the sample pressure from the velocity history, including backward hydrodynamic characteristics analysis,[46,47] iterative forward (IF) analysis[48] with radiation-hydrodynamics simulations, or an impedance-matching (IM) analysis[49] to constrain the pressure in the diffracting sample. This paper will focus on ramp-compression and the backwards characteristics approach, in particular, for these multi-layer targets. Discussion of IF and IM analyses are covered in detail elsewhere. Note that in this document, pressure P is used interchangeably with the longitudinal stress parallel to the stress wave propagation σ_{zz}.

For both opaque and transparent windows, the measured velocity serves as a boundary condition for a backward-characteristics analysis where the material flow is mapped as a grid of intersections of positive and negative characteristics. For opaque windows, stress waves are back-propagated through the window from the measured free-surface velocity $u_{fs}(t)$ to the sample layer using knowledge of the window EOS (see Fig. 15). For transparent windows, the sample–window particle velocity $u_p(t)$ is measured, after correcting for the refractive index of the window, and knowledge of the window and sample EOS is assumed to back-propagate

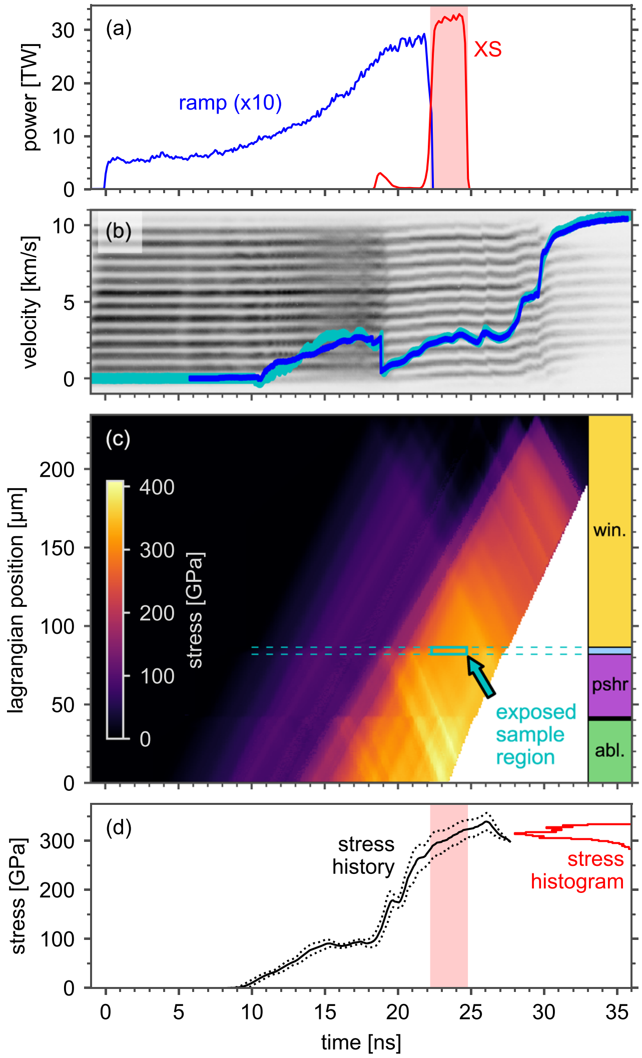

FIG. 15. NIF shot N150525-001, with a tantalum sample and a diamond window. (a) Laser power history for the sample assembly ramp drive (blue curve) and x-ray source (XS, red curve). (b) VISAR channel B streak record, approximately 0.4 mm across, and velocity histories for channels A (dark blue curve) and B (light blue curve). At about 19 ns, the dominant reflector switches from the sample–window interface to the window free surface. (c) Characteristics analysis of VISAR record giving longitudinal stress throughout the sample assembly. The blue box indicates the spatiotemporal area of the sample during x-ray exposure. Material layers are indicated on the right. (d) Sample-averaged stress (solid curve) and standard deviation (dotted curve) within the sample. The shaded red band indicates the period of x-ray exposure. A mass-weighted histogram of sample stress states during this period is plotted in red with a mean and standard deviation of 315 ± 10 GPa.

stress waves throughout the sample as a function of position and time.

Single-crystal diamond has been commonly used for the ablator, pusher, and window layers. The stress-density and sound speed for diamond have been measured to 5 TPa under ramp-compression conditions.[12,50] Its stiffness allows the ramp compression to be maintained over relatively large distances without steepening into a shock. Diamond's high strength results in an elastic wave of approximately 100 GPa that runs ahead of the main inelastic compression wave. For pressures above the elastic limit, diamond becomes opaque. While diamond is very strong under compression, with a yield strength near 80 GPa, it has comparatively low tensile strength. In our experiments, after pressure-release waves reach the free surface, tensile stresses are generated in the diamond and a spall layer may be produced.[51] Therefore, at late times, if such a layer is formed, the VISAR measures the velocity of this spall layer, whose signature is constant velocity, marking the end of the free-surface velocity measurement for pressure determination.

LiF and MgO are two commonly used transparent window materials. LiF is used because it is transparent under ramp compression up to at least 900 GPa[52,53] and is transparent under shock compression to 215 GPa.[54–56] Similarly, the optical and mechanical responses of LiF under ramp compression have been well characterized at Sandia's Z machine and at the NIF.[53,56,57] MgO is sometimes chosen as a window material because it was measured to be transparent under shock compression up to 226 GPa[58] and under ramp compression to even higher pressures, and it has a higher hydrodynamic impedance than that of LiF. When using a MgO window, it is recommended to remain under 600 GPa, where MgO undergoes a B1–B2 phase transformation,[15] to avoid loss of window transparency.

Using the backward-characteristics technique and bearing in mind the possibility of spall, a simplifying assumption that the pressure history in the sample is equal to the back-propagated diamond stress at the sample layer position can often be used. This includes no explicit treatment of the sample EOS or of wave reverberations between the sample, epoxy, and tamper layers. More-detailed calculations and hydrodynamic code simulations show this assumption to be valid during the sample hold period of most experiments (i.e., at times between 22 ns and 26 ns in Fig. 15), where sustained pressure equilibrium across the diamond–sample interfaces is achieved after multiple sample reverberations. However, for shots where the sample is very thick, or for shots where x rays probe the sample during the ramp compression portion of the drive (earlier than 21 ns in Fig. 15), we achieve improved accuracy in the sample pressure determination when reverberations are explicitly treated.

A more-sophisticated characteristics analysis approach allows for back-propagation through multiple material interfaces, which enables one to model wave reverberations in time and space. This eliminates the requirement of a monotonically increasing free-surface or particle velocity, as seen in Fig. 15(b), by interpolating in time, rather than in velocity. This allows for treatment of multiple negative slopes or "pull-backs" in free-surface velocity profiles.

The output of either characteristics analysis is a stress map in *h*-*t* space throughout the target [Fig. 15(c)], allowing one to estimate the spatial and temporal gradients in the sample during the x-ray exposure. The estimated sample pressure is characterized by an ensemble of pressures within the sample layer over the x-ray probe period, represented by a histogram of pressures in Fig. 15(d) (red curve) and described in detail in Sec. IV E 1.

IV. PERFORMANCE

This section discusses the performance attributes of the system, including a calculation of the photon throughput, the instrumental broadening, and the uncertainties in the scattering angle, lattice spacing, and pressure determinations.

A. Photometrics

As discussed above, a scanned area detector produces an array of pixel values D that can be described as the sum of the signal S and the total background B,

$$D = S + B. \tag{24}$$

Section III D describes an estimate of the background B to recover the signal S. The signal S, in turn, can be decomposed into a product of the sample response R and a factor dependent on the system geometry G,

$$S(2\theta, \alpha, \beta, \psi) = R(2\theta) G(\alpha, \beta, \psi). \tag{25}$$

As above, 2θ is the x-ray scattering angle, α and β are the entrance and exit angles, respectively, of the x-ray path compared to the sample normal, and ψ is the x-ray incidence angle on the detector with respect to the detector normal. This breakdown bundles all the "physics" of the sample into R and the remaining experimental geometry factors into G, which can be computed independent of the behavior of the sample. Section IV A 1 will describe an *ab initio* estimate of R.

The geometric response G of the experimental setup can in turn be expressed as the product of independent terms originating from the x-ray source, sample assembly, pinhole, and detector,

$$G = I_0(\alpha) H_s(\alpha, \beta) A_p(\beta) W_d(\psi), \tag{26}$$

where I_0 is the x-ray fluence incident on the sample from the x-ray source (Sec. IV A 2); H_s is the effective thickness of the sample assembly, as described in Sec. IV A 3; A_p is the effective pinhole area (Sec. IV A 4); and W_d is the detector response function (Sec. IV A 5).

1. Sample x-ray response factor

Formulae for the integrated power of reflection of x rays have long been known and are readily available from numerous sources. The International Tables for Crystallography[59]—one such source—report the integrated power of reflection from an ideal powder in Table 6.2.1.1,

$$\frac{P}{I_0} = \frac{r_e^2 \lambda^3 V}{V_C^2} M|F|^2 \frac{1 + \cos^2 2\theta}{8 \sin\theta}. \tag{27}$$

This expression assumes the kinematic (single-scattering) limit and no absorption in the sample. Here, I_0 is the incident intensity, P is the diffracted power, $r_e = (\mu_0/4\pi)(e^2/m_e) = 2.818 \times 10^{-15}$ m is the classical radius of the electron, λ is the x-ray wavelength, V is the volume of the sample, V_C is the volume of a unit cell in the sample's crystalline lattice, M is the multiplicity factor, F is the structure factor, and 2θ is the angle between the incident and scattered beams.

The structure factor F is the ratio of the amplitude of scattering by one unit cell in the lattice to that of a free electron. It is calculated by summing over the contributions of the N individual atoms that make up the unit cell, keeping track of the relative phase. The structure factor for the $\{hkl\}$ reflection is

$$F_{hkl} = \sum_{j=1}^{N} f_j(q) e^{-B_j(q)} e^{i\vec{q}_{hkl}\cdot\vec{r}_j}, \tag{28}$$

where $\vec{r}_j$ is the position vector of the jth atom within the unit cell and $\vec{q}_{hkl}$ is the wavevector satisfying the Bragg condition for the given $\{hkl\}$ Miller indices,

$$q = 2\pi/d = 4\pi(\sin\theta)/\lambda, \tag{29}$$

for first-order reflections. Here, d is the spatial period of the lattice planes satisfying the Bragg condition.

The atomic form factor (f_j) is the ratio of the scattering amplitude from the jth atom compared to that of a free electron. Tables and interpolation formulas for f_j as a function of scattering wave number (q) are available from numerous sources (e.g., Ref. 59). The Debye–Waller term e^{-B_j} accounts for the typical displacement of the jth atom from its ideal location due to temperature or other imperfections and is equal to 1 for a perfect crystal at zero temperature.

The effective volume V differs substantially across the detector for this experiment, depending primarily on the system geometry. This effective volume is assigned to be a component of the geometric response G and is a product of an effective sample thickness H_s, including absorption in the sample, and an effective area A_p due to the pinhole, described in Secs. IV A 3 and IV A 4, respectively.

The sample response function R used in Eq. (25) is

$$R = \frac{r_e^2 \lambda^3}{V_C^2} M|F|^2 \frac{1 + \cos^2 2\theta}{8 \sin\theta \sin 2\theta} X(2\theta) \tag{30}$$

and can be interpreted as the total differential cross section per steradian per unit volume of the sample. The extra factor of $\sin 2\theta$ accounts for the different length of a Debye–Scherrer ring as a function of 2θ, and the function $X(2\theta)$ is a normalized line shape function. The line shape is often approximated as a Gaussian,

$$X(2\theta) = \frac{1}{\sqrt{2\pi\sigma^2}} \exp\left[-\frac{(2\theta - 2\theta_B)^2}{2\sigma^2}\right], \tag{31}$$

where θ_B is the Bragg angle for the $\{hkl\}$ reflection and σ is the combined instrumental 2θ broadening, described in Sec. IV B.

2. X-ray yield and incident fluence

The energy yield Y_x of the x-ray source is

$$Y_x = E_{\text{laser}} \epsilon_{\text{foil}}, \tag{32}$$

where E_{laser} is the total incident energy of the laser and ϵ_{foil} is the XSF conversion efficiency of laser energy into He$_\alpha$ emission of the foil material. In general, ϵ_{foil} is a function of the laser irradiance, laser spot size, and foil material. For typical drive parameters at OMEGA and the NIF, $\epsilon_{\text{foil}} = 1\%$ is commonly observed.[33,34]

The XSF is offset a distance r_x from the center of the pinhole and at a zenith angle α with respect to the sample normal and pinhole

TABLE III. Parameters for typical diffraction x-ray sources at OMEGA and the NIF.

Facility		Ω	NIF
Foil material		Cu	Ge
Photon energy (keV)	$h\nu$	8.37	10.25
Laser drive energy (kJ)	E_{laser}	5	80
Laser spot size (mm)	d_{laser}	0.5	0.3
Laser irradiance (PW/cm^2)	I_{laser}	1.1	3
X-ray He$_\alpha$ line yield (J)	Y_x	50	800
X-ray source distance (mm)	r_x	24	32
X-ray source angle (deg)	α	45	30
He$_\alpha$ fluence at the sample (10^{18} photons/m^2)	I_0	4	33

axis. The x-ray photon fluence I_0 incident on the sample and normal to its surface is

$$I_0 = \frac{Y_x}{h\nu}\frac{\cos\alpha}{4\pi r_x^2}, \tag{33}$$

where $h\nu$ is the mean He$_\alpha$ photon energy. Table III summarizes the typical x-ray source parameters for Cu and Ge foils at OMEGA and the NIF, respectively.

3. Effective thickness of the sample including absorption

The intensity of scattered x rays is directly proportional to the thickness of the scattering sample, h_s, if x-ray absorption in the sample material is negligible. For non-negligible sample x-ray attenuation, some portion of the x rays will be absorbed, thereby reducing the diffraction signal on the detector. The effective thickness for x-ray scattering, H_s, depends on the incident and the exit angles with respect to the sample normal,

$$H_s(\alpha,\beta) = h_s T_s(\alpha,\beta). \tag{34}$$

The total transmission of the sample assembly, T_s, is the product of the transmissions of the ablator and any other layers in front of the sample, the sample layer itself, and the window and any other layers behind the sample,

$$T_s(\alpha,\beta) = T_{\text{abl}}(\alpha)T_{\text{smp}}(\alpha,\beta)T_{\text{win}}(\beta). \tag{35}$$

The transmission of "ablator" and "window" stacks is easily related to the transmission at normal incidence, T_0,

$$T = T_0^{\sec\eta}, \tag{36}$$

where η represents α or β for the ablator and window stacks, respectively.

Transmission through the sample will use a similar expression to that of Eq. (36) only in the case where $\alpha = \beta$, which includes forward-scattering ($2\theta = 0$) and two additional points if $2\theta < 2\alpha$,

$$T_{\text{smp}}\big|_{\alpha=\beta} = e^{-\mu_s h_s \sec\alpha}, \tag{37}$$

where μ_s is the wavelength-dependent linear attenuation coefficient and h_s is the thickness of the sample layer. In general, however, scattering of the diffracted x ray within the sample will not result in an exit angle equal to the incident angle. Here, we will consider the single-scattering kinematic limit and neglect the contribution due to multiple scattering within the sample.

Consider an x-ray that scatters within an absorbing planar slab of total thickness h_s at a depth z from the front surface and at a scattering angle 2θ with respect to the incident vector (Fig. 16). The relation between α, β, and 2θ is

$$\cos(2\theta) = \cos\alpha\cos\beta - \sin\alpha\sin\beta\cos(\Delta\phi), \tag{38}$$

where $\Delta\phi = \phi_x - \phi_d$ is the azimuthal angle difference between the incident and exit vectors.

The transmission T_z of the scattered x-ray signal from depth z in the sample is related to the attenuation it incurs as it traverses the sample layer,

$$T_z = e^{-\mu_s s}, \tag{39}$$

where the total path length s in the sample layer is

$$s = s_1 + s_2 = \frac{z}{\cos\alpha} + \frac{h_s - z}{\cos\beta}. \tag{40}$$

The transmission factor averaged over the sample layer, T_{smp}, is calculated by averaging T_z over the x-ray scattering depth,

$$T_{\text{smp}} = \frac{1}{h_s}\int_0^{h_s} T_z dz. \tag{41}$$

Combining terms from previous equations, this integral is readily integrated,

$$T_{\text{smp}} = \frac{1}{\mu_s h_s}\frac{e^{-\mu_s h_s \sec\alpha} - e^{-\mu_s h_s \sec\beta}}{\sec\beta - \sec\alpha}. \tag{42}$$

To maximize the diffraction signal on the detector, one must balance the increased absorption of a thicker target against its larger scattering volume. The optimum thickness for many configurations is in the vicinity of one optical depth (see Fig. 17).

An interesting and useful consequence of the inverse relation of the sample density and x-ray attenuation coefficient is that for

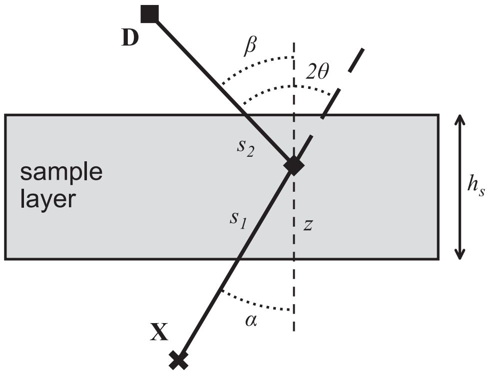

FIG. 16. Geometry for a diffracting absorbing slab of total thickness h_s, where an x-ray beam from source **X** is incident at an angle α to the slab normal, diffracts at depth z, and exits at zenith angle β toward the detector element **D**.

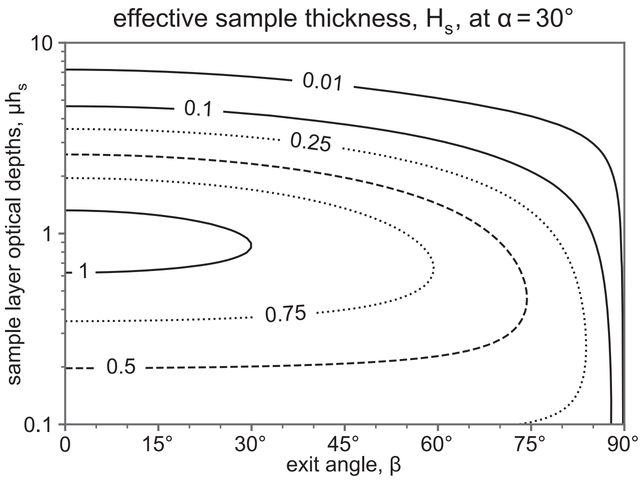

FIG. 17. Effective scattering thickness, H_s, from an absorbing sample layer vs exit angle β for an entrance angle $\alpha = 30°$. H_s contours are normalized by the signal from a sample thickness of one optical depth ($\mu_s h_s = 1$) at $\alpha = \beta = 0$.

uni-axial compression, as is the case here, the effective thickness H_s is independent of the amount of compression.

4. Effective aperture area

The x rays traveling through the cylindrical aperture toward the detector experience an effective pinhole area according to their angle of incidence (equivalent to the exit angle β from the sample assembly). The finite substrate thickness h_p of a pinhole of diameter d_p reduces the effective pinhole area A_p from the infinitely thin value of $(\pi d_p^2/4)\cos\beta$ to that of the intersection of two ellipses offset along their minor-axis (Fig. 18),

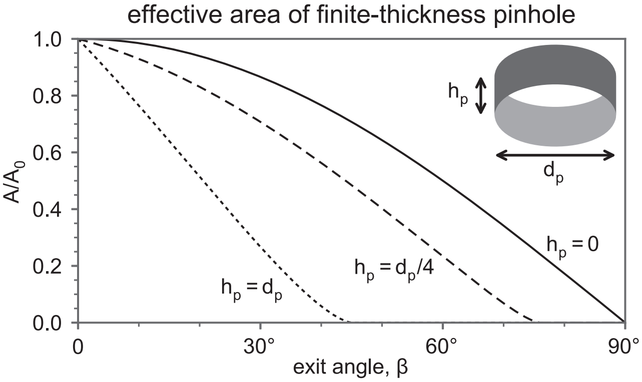

FIG. 18. Effective area of a finite-thickness cylindrical aperture in a fully opaque substrate vs exit angle β, normalized to A_0, the area at $\beta = 0$. As the aspect ratio (thickness h_p over diameter d_p) of the pinhole approaches zero, the effective area approaches $A_0 \cos\beta$. The critical angle at which the effective area reaches zero is given by $\tan\beta_{\mathrm{crit}} = d_p/h_p$.

$$A_p = \frac{d_p^2}{2}\cos\beta\left[\tan^{-1}\left(\sqrt{J^{-2}-1}\right) - J\sqrt{1-J^2}\right], \qquad (43)$$

where $J = J(\beta) = (h_p/d_p)\tan\beta$.

This expression assumes that the pinhole substrate is completely opaque to the x rays of interest. Considering the linear attenuation μ_p of the aperture substrate to these x rays will introduce a correction to the effective area of order $1/(\mu_p d_p)^2$. For example, for Ge He$_\alpha$ x rays through a Ta aperture ($1/\mu_p = 2.7$ μm and $d_p = 400$ μm), this correction is much less than 1%.

5. Detector response function

The detector response function is calculated on a per-pixel basis as the product of the pixel solid angle, the transmission of any filters in front of the detector, and the x-ray sensitivity of the detector medium,

$$W_d(\psi) = \Omega_d(\psi)T_d(\psi)Q(\psi), \qquad (44)$$

where ψ is the incident angle with respect to the detector element normal. The transmission T_d and the sensitivity Q are, in general, also dependent on the energy $h\nu$ of the incident x rays. However, assuming the background is appropriately subtracted, we can evaluate the sensitivity at the energy corresponding to the signal wavelength, $h\nu = hc/\lambda$.

After passing through the pinhole, x rays encounter a detector element (such as an image plate pixel) of area A_d, at a distance of r_d from the pinhole center, and at an incident angle ψ with respect to the detector element normal. The solid angle (in steradians) of the detector element is

$$\Omega_d = \frac{A_d}{r_d^2}\cos(\psi). \qquad (45)$$

X rays will also pass through a filter (or filters) aligned parallel to the detector element. Filters are inserted to protect the detector from debris and to attenuate low-energy background photons. If the transmission of all filters at normal incidence is T_0, the transmission at incident angle ψ is

$$T_d(\psi, h\nu) = T_0(h\nu)^{\sec\psi}. \qquad (46)$$

The spatial distribution of x rays is recorded on Fujifilm™ BAS–MS image plates (IP's).[40,60–62] The IP's store incident x-ray energy in phosphor elements that are then read into units of photo-stimulated luminescence (PSL) using a calibrated[63] scanner. IP's have broad spectral sensitivity, a linear response to x-ray fluence, and a high dynamic range; they are also insensitive to radio-frequency electromagnetic noise.

One physical model[61,62] of the image-plate's x-ray sensitivity Q in PSL/photon is that Q is proportional to the deposited energy, with a correction applied for the readout depth of the phosphor element,

$$Q = U_0 \int_0^{h_d} \frac{dE(z, h\nu)}{dz} e^{-z/L} dz, \qquad (47)$$

where h_d is the thickness of the detector phosphor layer ($h_d = 115$ μm for MS-IP), dE/dz is the deposited energy per unit depth, and L and U_0 are fitting parameters corresponding to the characteristic readout depth of the phosphor and to the base sensitivity of the image plate/scanner setup.

For MS–IP's, we have $L = 222 \pm 73\ \mu$m and $U_0 = 0.695 \pm 0.126$ PSL/MeV for user scan settings of sensitivity S4000, latitude L5, and scan resolution 50 μm.[61] We typically use the 100-μm scan resolution setting, giving $A_d = 0.01$ mm^2. For this setting, U_0 and, therefore, Q should be multiplied by 1.38 to adjust for the different overscan compared to the reference 50-μm scan resolution setting.[40] The signal is also adjusted according to the fade curve[40] based on the time interval between the exposure and the start of the scan.

A complete calculation of the energy deposition includes all interactions of the incident x rays with the detector in addition to energy deposition from any secondary radiation. This calculation has previously been performed for x rays at normal incidence with favorable comparison to experimental sensitivities using various Monte Carlo codes such as Geant4[61] and MCNPX.[62]

In our experimental geometry, x rays are incident on the IP at a variety of incident angles. In addition, we note that for photons up to moderate energies ($h\nu < 100$ keV), x-ray interactions with the IP phosphor layer are dominated by photoelectric absorption. We can thus construct an analytic expression for the energy deposition argument,

$$\frac{dE(z,h\nu)}{dz} = h\nu\mu_d \sec(\psi)\exp(-\mu_d z \sec\psi), \tag{48}$$

where μ_d is the $h\nu$-dependent linear absorption coefficient in the phosphor and $\sec\psi = 1$ at normal incidence. Using the composition and density of the MS–IP phosphor layer reported previously,[40,60,61] we obtain $\mu_d = 1/(30\ \mu\text{m})$ at 10.25 keV. Corrections to the energy deposition due to fluorescence losses should also be included for photon $h\nu$ above the Br, I, and Ba K-edges at 13.5 keV, 33.2 keV, and 37.4 keV, respectively. MS–IP's have a 9 μm plastic layer in front to protect the phosphor layer; the sensitivity should further be corrected for the transmission through this layer in the same fashion as for the detector filters [see Eq. (46)]. For 10.25 keV photons, this correction is negligible (99.5% transmission).

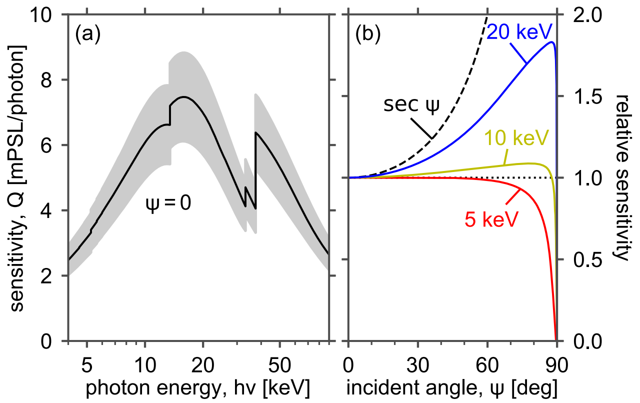

FIG. 19. (a) Photon sensitivity for BAS-MS image plates (IP) vs photon energy at normal incidence for an FLA7000 scanner with scan settings of S4000, L5, and 50-μm pixel size. The gray band indicates the systematic model uncertainty. (b) IP relative sensitivity vs incident angle, normalized to normal incidence. The sensitivity is independent of the incident angle for photons that are fully absorbed in the phosphor layer, except at very low photon energies, where absorption in the IP cover layer is evident for high incidence angles. At higher photon energies, the sensitivity approaches the sec ψ dependence characteristic of volumetric (optically thin) detection.

Combining the previous two equations and integrating the result, we get an analytic expression for the IP sensitivity as a function of incident angle and photon energy, again up to about 100 keV (see also Fig. 19),

$$Q(\psi,h\nu) = U_0 h\nu \frac{1 - \exp\left[-\mu_d h_d\left(\sec\psi + \frac{1}{\mu_d L}\right)\right]}{\sec\psi + 1/(\mu_d L)}. \tag{49}$$

At normal incidence, this expression shows good agreement with experimental data and Monte Carlo models below 100 keV. The dependence of IP sensitivity on the incidence angle moves from no angle dependence (surface detection) for low energies where $\mu_d h_d < 1$ toward secant angle dependence (volume detection) for higher energies where $\mu_d h_d \gg 1$. In the latter case, the energy deposition at glancing incidence will distribute energy over more scan pixels and will also degrade spatial resolution in that direction. We also note that for high incidence angles and low photon energies, absorption in the IP surface layer will reduce the effective sensitivity.

6. Combined geometric response

As described above, the geometric response G was decomposed into a number of terms related to the x-ray source, sample layer, pinhole, and detector,

$$G(\alpha,\beta,\psi) = I_0(\alpha)H_s(\alpha,\beta)A_p(\beta)W_d(\psi). \tag{50}$$

Again, by construction, G is independent of the 2θ scattering angle. However, the value of G displays significant variation over the detector area, and the overall sensitivity of the platform does depend on 2θ, as shown in Fig. 20.

The units of G are PSL-meter-steradian, deduced from the component incident x-ray irradiance I_0 (photons/m^2), the effective sample thickness (m), the effective aperture area (m^2), and the detector response (sr PSL/photon). The product of G with the sample response R [Eq. (30)] gives the signal in PSL. In some cases, the measured signal is divided by G in order to give an estimate of R. This step is unnecessary for determining diffraction line scattering angles, but it becomes important for analyses that rely on the absolute or relative scattering intensity of the lines.

B. Instrumental broadening

The total 2θ instrumental broadening σ is due to a convolution of several independent broadening sources. We will treat the convolution here as the quadrature sum of the various terms. However, in cases where the details of the line shape are important, the convolution of the individual contributions should be considered in more detail since not all components are well described by Gaussian distributions.

1. Spectral broadening

For a small width σ_λ in the wavelength around a central wavelength λ, a Taylor expansion of Bragg's law gives the angular resolution σ_θ,

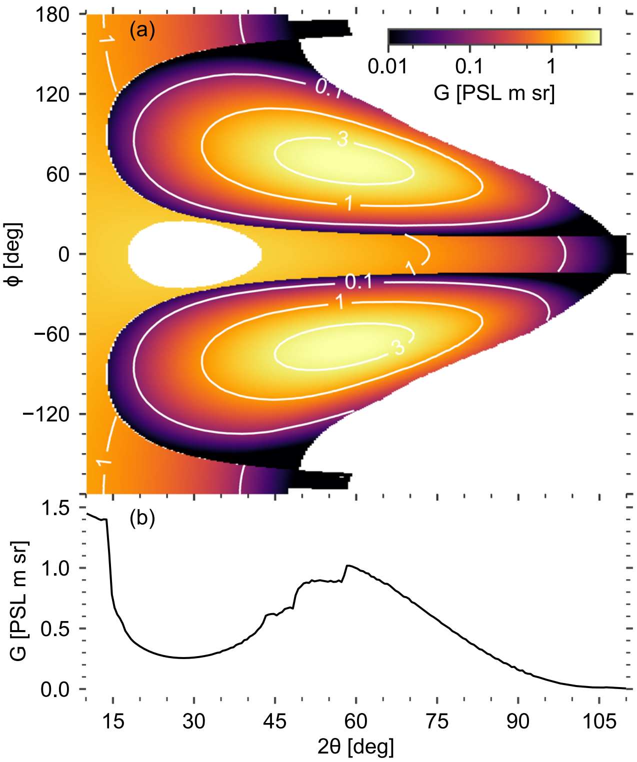

FIG. 20. (a) Geometric response *G* of the standard TARDIS experimental configuration. (b) Azimuthally averaged geometric response.

$$\sigma_\theta = \frac{n}{2d\cos\theta}\sigma_\lambda. \tag{51}$$

The x-ray scattering angle 2θ is twice the Bragg angle. The broadening of the x-ray scattering angle can be expressed in terms of the fractional wavelength line width, σ_λ/λ,

$$\sigma_{2\theta,\lambda} = 2\frac{\sigma_\lambda}{\lambda}\tan\theta. \tag{52}$$

The x-ray source spectral width is typically dominated by the separation of the He$_\alpha$ lines, of order 0.5%.

2. Geometric broadening

Several geometric factors contribute to the broadening of the lines in 2θ, including the source size, pinhole size, distance between the source and the pinhole, distance between the pinhole and each detector element, and point response of the detector.

Consider an x-ray source with spatial extent d_x at a distance r_x and an angle α from the axis of a cylindrical pinhole of diameter d_p in an opaque substrate of thickness h_p. An x ray scatters at an angle 2θ from a sample near the pinhole, exiting at an angle β from the pinhole's axis. It encounters a detector element of size d_d at a distance r_d from the aperture at an angle ψ from the detector normal.

The size of the pinhole creates a range of angles seen by both the source and the detector; however, these two contributions are correlated. Let us initially restrict our consideration to detector elements that are within the plane defined by the initial x-ray vector and the aperture axis and to aperture substrates with vanishing thickness. In this case, the exit angle is given by $\beta = 2\theta \pm \alpha$, with the sign indicating the direction of scattering (away from or toward the axis). Broadening in 2θ due to the pinhole size is then

$$\sigma_{2\theta,p} = \frac{d_p}{2r_x}\cos\alpha + \frac{d_p}{2r_d}\cos\beta. \tag{53}$$

The finite thickness of the aperture substrate will act to reduce its effective size dependent on the exit angle, $d_p \to d_p[1 - (h_p\tan\beta)/d_p]$, and will go to zero at the critical exit angle, $\beta_{\rm crit} = \arctan(h_p/d_p)$.

The broadening due to the finite extent of the x-ray source and the detector elements is calculated according to the apparent extent of the objects with respect to the diffracting sample. In the small angle limit ($d \ll r$), they scale like d_x/r_x and $(d_d/r_d)\cos\psi$, respectively.

The combined geometric broadening is now calculated as the quadrature sum of these three finite-size terms,

$$(\sigma_{2\theta,\rm geom})^2 = (\sigma_{2\theta,p})^2 + \left(\frac{d_x}{2r_x}\right)^2 + \left(\frac{d_d}{2r_d}\cos\psi\right)^2. \tag{54}$$

The total broadening is not uniform across the detector area. Figure 21 shows the total broadening over the entire detector.

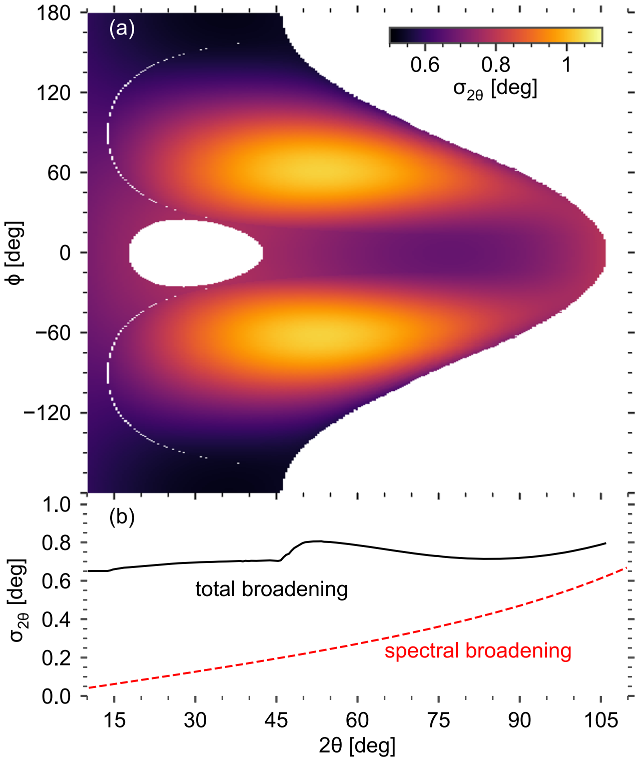

FIG. 21. (a) Total instrumental broadening (1-σ) of scattering angle 2θ for standard TARDIS geometry, including geometric and spectral broadening terms. (b) Azimuthally averaged total broadening (black curve). The spectral broadening component (red curve) is independent of ϕ.

The broadening in 2θ due to the finite thickness of the sample is small (<0.01°), so is neglected.

3. Pressure histogram broadening

A dynamically driven sample will, in general, have some distribution of pressures σ_P around the average pressure P. Both spatial nonuniformity of the drive pressure and temporal evolution of the pressure over the duration of the x-ray exposure will contribute to this pressure distribution and its complementary density distribution (see Sec. IV E 1). For the purpose of estimating the pressure histogram, we will use a mechanical equation of state (EOS), $\rho = \rho(P)$, where the EOS is determined from either theoretical tables or previous ramp experiments.[12,50]

Assuming isotropic compression (i.e., stress tensor is diagonal with equal components), the lattice spacing d scales with the density ρ like

$$\frac{d}{d_0} = \left(\frac{\rho}{\rho_0}\right)^{-1/3}, \tag{55}$$

from which small fractional changes scale as

$$\frac{\sigma_d}{d} = -\frac{1}{3}\frac{\sigma_\rho}{\rho} = -\frac{1}{3\,K(P)}\sigma_P, \tag{56}$$

where $K(P)$ is the pressure-dependent bulk modulus. This can be converted to an x-ray scattering angle after application of Bragg's law,

$$\sigma_{2\theta} = -2\frac{\sigma_d}{d}\tan\theta, \tag{57}$$

or in terms of pressure variation,

$$\sigma_{2\theta,P} = \frac{2}{3}\frac{\tan\theta}{K(P)}\sigma_P. \tag{58}$$

C. Scattering angle uncertainty

The 2θ scattering angle of peaks observed on the detectors depends on the relative positions of the x-ray source, pinhole, and detector. Engineering and metrology tolerances on the diagnostic hardware constrain the maximum 2θ uncertainty to less than 1° over most of the detector area. However, the experimental geometry is determined to greater precision than engineering tolerances using the forward-scattered image, shadows from various internal hardware, and the observed diffraction curves themselves, as described above in Sec. III A. Scattering angle adjustments due to the fitted geometry are typically a few tenths of a degree compared to the nominal configuration.

Empirical determination of the 2θ scattering angle precision (Fig. 22) was obtained by comparing the angles of observed peaks analyzed by two different users (A and B) from two different experiments (a and b) and with up to two different x-ray exposures (1 and 2). The two users independently analyzed the same raw experimental data using two separate software implementations of the analysis algorithms described herein. The experiments used germanium x-ray source foils to expose [experiment (a)] a lead foil at zero pressure, producing six observed diffraction peaks, and [experiment (b)] a platinum foil compressed to 180 GPa with dual co-timed x-ray pulses (1 and 2), producing five observed diffraction peaks.

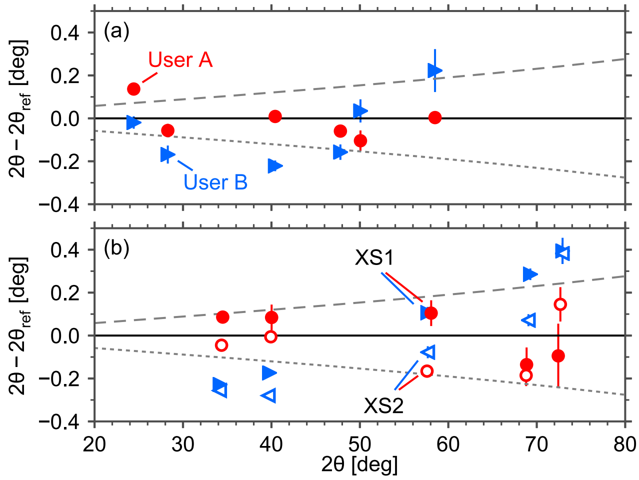

FIG. 22. Difference between observed 2θ scattering angle and reference angle for each scattering peak for given a/λ, with λ = 1.209 Å, the average of the Ge He$_{\alpha 1,2}$ wavelengths. The analysis was performed independently by two different users (user A: circles; user B: triangles). (a) Shot N160518-001, ambient lead with an fcc crystal structure and a = 4.951 Å. (b) Shot N160517-003, a dual, co-timed x-ray source (XS) exposure of fcc platinum compressed to a = 3.542 Å at 180 GPa. Closed (open) symbols are the results from XS-1 (XS-2). Dashed and dotted lines show the angular difference for the 0.57% wavelength separation between the Ge He$_{\alpha 1}$ and He$_{\alpha 2}$ lines, respectively.

The results of this study are shown in Fig. 22, where the observed 2θ is compared to a reference 2θ angle expected for scattering from an fcc lattice with lattice constant a/λ = 4.095 or 2.929 for (a) and (b), respectively. The standard deviation of measured angles compared to the respective reference is 0.2° or better, with comparable angular agreement for two different experiments, and between two different users, and for two different x-ray exposures.

D. Lattice spacing uncertainty

The uncertainty in the inferred lattice spacing comes primarily from the uncertainty in the observed 2θ scattering angle, with an additional contribution from the uncertainty in the x-ray source mean wavelength. The differential expansion of Bragg's law gives the relative uncertainty in the lattice spacing d for first-order reflections,

$$\left(\frac{\delta d}{d}\right)^2 = \left(\frac{\delta\lambda}{\lambda}\right)^2 + [\cot(\theta)\delta\theta]^2, \tag{59}$$

where the refractive index is approximated as 1 for these short-wavelength x rays.

The 2θ precision of 0.2° discussed in Sec. IV C (also see Fig. 22) results in a fractional lattice d-spacing uncertainty of several parts per thousand, depending on the scattering angle. For example, a single line detected at $2\theta = 45°$ gives $\delta d/d \approx 0.004$. When fitting multiple lines to a candidate structure, the relative uncertainty in the crystal lattice constant(s) may be reduced even further, depending on the complexity of the structure.

K-shell transition wavelengths in helium-like period 4 elements are known to a few tens of parts per million,[64,65] while the separation between individual transitions within the emission complex is of the order of one part in 100. The individual transitions are not resolved in our diffraction setup, so the wavelength contribution to uncertainty is due primarily to the uncertainty in the relative emission from these transitions and from nearby satellites (e.g., K-shell emission from lithium-like and beryllium-like ions).

The two dominant components of this He_α complex are the electric dipole transitions from the $1s2p(^1P_1,\ ^3P_1)$ states to the $1s^2(^1S_0)$ ground state, known also as the $\mathrm{He}_{\alpha 2}$ "resonance" and the $\mathrm{He}_{\alpha 1}$ "intercombination" lines (or the w and y lines in the Gabriel notation). The *ab initio* calculation of the relative emission of these lines and of nearby satellites is very challenging due to large gradients, rapid evolution, and nonequilibrium properties of laser-driven plasmas.

Determination of the mean wavelength is based instead on *in situ* spectral measurements of the x-ray source (see Sec. II E), which have measured the mean wavelength of the complex down to one to two parts per thousand.[34] These measurements are all consistent with a mean energy equal to the average of the $\mathrm{He}_{\alpha 1,2}$ wavelengths. For a germanium XS foil, this gives $\lambda_0 = 1.2095 \pm 0.002$ Å.[34,66] The corresponding fractional uncertainty in d is also about two parts per thousand.

To evaluate the absolute uncertainty in determining the lattice constant of cubic systems, NIF experiment N160518-001 included exposure of an undriven lead sample with a Ge x-ray source. The results of N160518-001 shown in Fig. 22(a) give $a = 4.954 \pm 0.011$ Å, which includes the uncertainty in the mean wavelength and scattering angles of the six observed lines. This value differs from the reference value (Ref. 67) of 4.9508 ± 0.0001 Å for lead at ambient pressure and 298 K by 0.003 Å. This confirms that this platform can measure the lattice constant with an accuracy of order two parts per thousand or better.[68] This corresponds to a density uncertainty of six parts per thousand or better.

E. Pressure uncertainty

As described in Sec. III F, dual-channel VISAR measurements of the free-surface or sample–window-interface velocity are used to infer the longitudinal stress in the sample. We will here continue to approximate the deviatoric response of the sample as small and use pressure and longitudinal stress interchangeably. One exciting avenue of future research is to evaluate the deviatoric response of different samples to various extreme loading conditions, but that topic is beyond the scope of this discussion.

For a well-designed experiment, the total uncertainty in pressure can be split into about 1% random uncertainty and 3% systematic uncertainty. Additional uncertainty contributions can arise if the sample is driven far above the calibration pressure of the window material, if the x-ray source is mistimed with respect to the pressure plateau, or if an intended pressure ramp steepens up to form one or more shocks before being recorded by the VISAR.

The primary source of random uncertainty comes about due to the uncertainty in determining the phase of the VISAR fringes. In a high-quality VISAR record at the NIF, fringe phase can be determined to about 2% of a fringe (i.e., 7°). VISAR etalons for these experiments are typically selected so that the maximum fringe shift on the more sensitive etalon is about five fringes, giving an overall precision in the measurement of the maximum velocity of a bit smaller than 1%, translating to a pressure uncertainty of approximately 1%. A low-reflectivity target or the presence of strong VISAR "ghost fringes" can increase this uncertainty contribution considerably.[45]

An unavoidable source of systematic uncertainty arises from the current calibration of the mechanical response of the window materials at high pressures. The pressure–density equation of state (EOS) under ramp compression has been measured at the 3% level up to 800 GPa in single-crystal diamond,[50] to 825 GPa in LiF,[53,56] and to about 900 GPa in MgO.[15] Additional pressure–density data under ramp loading with a small initial shock has been reported up to 5000 GPa in nanocrystalline diamond.[12] For MgO, the pressure–density at the highest pressures was measured using the current platform (PXRDIP at Omega-60), with the pressure determined based on the single crystal diamond response. Evaluation at higher pressures requires extrapolating beyond the range of current experimental data, often by using theoretical EOS's that match the available experimental data.

Interface velocity measurements recorded through transparent windows must furthermore include a correction due to the difference between the apparent and true velocities, typically through measurements of the refractive index. Measurement of the refractive index of LiF is available up to several hundred GPa,[52,53] with uncertainties down to 0.3%.[56] The refractive index of MgO has been measured under shock compression up to 226 GPa to a precision of about 0.7%.[58] As with the mechanical response, the optical response of these materials at pressures higher than previous measurements requires theoretical extrapolation, with an ensuing increase in the systematic uncertainty.

Back propagation of the free-surface velocity on experiments with diamond windows must furthermore include the significant strength of diamond in interpreting the sample pressure. This is an area of active investigation, with an early report yielding a systematic and non-symmetric error of up to 50 GPa.[20] For VISAR records ending at a high and steady velocity with diamond windows, the possibility of spall due to the relatively low tensile strength of diamond must also be considered.

For pressure–temperature load paths that differ substantially from those used for the mechanical and optical calibration of the windows, adjustments to the calibration due to differences in temperature are often appropriate.

An important attribute of the sandwich target geometry is that the final pressure under ramp compression and the determination of that pressure are nearly independent of (1) the EOS of the sample, (2) small uncertainties in the target layer thicknesses, (3) small uncertainties in the x-ray probe timing, and (4) small shock-like jumps in the velocity record.

This experimental attribute is most valid if the sample layer is thin enough that the reverberation time within the sample is smaller than the characteristic ramp time. For ramp compression over a time scale Δt_{ramp} of a sample with Lagrangian sound speed c_{L}, the sample EOS will not play a major role if the sample thickness $h_s \ll c_{\mathrm{L}}\Delta t_{\mathrm{ramp}}$. As h_s increases to be comparable to $c_{\mathrm{L}}\Delta t_{\mathrm{ramp}}$, the sample EOS will play an increasingly important role, eventually necessitating a treatment of the pressure wave through the sample, such as through the backward Lagrangian analysis like that used for a diamond window. For shock or shock-ramp compression, the sample

EOS is, of course, an essential component in designing the pressure history in the target.

For ramp experiments, sufficiently small shock events in the VISAR record can be treated within the ramp framework using the backward Lagrangian analysis, with a manageable addition to the pressure uncertainty.[69] However, if the shock events are relatively large compared to the total ramp drive, they will need to be treated explicitly. For example, a leading shock would then be handled as a shock-ramp instead of a ramp drive.

In these dynamic experiments, the pressure during x-ray exposure will not be precisely the same throughout the sample regardless of the loading path. The temporal and longitudinal sample pressure variation is deduced from the VISAR record on a shot-by-shot basis (see Sec. IV E 1) and can often be kept to less than a few percent. In addition, transverse nonuniformity arises due to the finite extent of the laser drive spot and has been characterized to be less than 5%, as described in Sec. IV E 2. It should be noted here that the pressure nonuniformity during x-ray exposure is an independent metric from the pressure uncertainty. For example, a large nonuniformity means that a wide variety of pressure states are contributing to the sample, which will primarily broaden the diffraction peak rather than increase the pressure uncertainty.

A well-designed ramp drive will hold the sample in a temporal plateau of pressure for a duration longer than the x-ray exposure, in which case timing uncertainties have a negligible contribution to the pressure uncertainty. In some cases, however, due to laser or material limitations, the plateau cannot be designed to be long enough. In other cases, mistiming can result in an x-ray exposure that does not coincide precisely with the pressure plateau.

In such cases, a full analysis of the pressure histogram (as described briefly above and in more detail in Sec. IV E 1), and including propagation of uncertainties, is often required. However, we can estimate the pressure deviation $\delta P \approx (P_2 - P_1)\delta t/\Delta t$, where δt is the timing deviation, Δt is the exposure duration, and P_1 and P_2 are the mean sample pressure at the beginning and end of the x-ray exposure, respectively. As remarked above, for a well-designed pressure plateau, $P_2 = P_1$ and the sample pressure is independent of small timing uncertainties.

The propagation of pressure uncertainties originating from target layer thicknesses and initial densities likewise requires the pressure histogram analysis. Again, the target assembly and metrology uncertainties make very small contributions to the pressure uncertainty for a well-designed experiment with a long pressure plateau.

1. Longitudinal and temporal uniformity

For ramp compression, the pressure as a function of time and depth $P(z, t)$ throughout the sample layer is deduced from the VISAR velocity record using the method of characteristics, as described in Sec. III F. In addition to determining the mean pressure, the pressure history can also be used to evaluate the distribution of pressures during the time of exposure.

A histogram of sample pressures exposed to the x-ray source is generated by binning up the $P(z, t)$ history, weighted by the amount of mass in the bin, the duration of the bin, and the power of x-ray emission at that time [see Fig. 15(d)]. In the simplest approximation, the sample is binned up into equal masses, and the x-ray exposure is taken over a square window of time during peak pressure. Additional precision can be obtained by using the measured emission history over an appropriate bandwidth (see Fig. 4) and applying systematic timing corrections (up to 100 ps) due to photon time-of-flight over the typical distances (up to 37 mm).

With the pressure histogram in hand, various moments of the distribution can be obtained, such as the mean and standard deviation. For a well-designed experiment, the standard deviation of pressures can be as low as a few percent.

We again emphasize that the width of the pressure distribution is not the same as the uncertainty in the mean pressure. The principal effect of a wide pressure distribution is to broaden the lines in 2θ. In rare cases, if the breadth spans a phase transition, it is possible to see lines from both phases. With multiple experiments, it is sometimes possible to disambiguate whether the presence of lines from two phases is actual coexistence rather than a broad histogram.[21] Experiments with very broad pressure histograms—due to mistiming, for example—are sometimes omitted from the ensemble.

2. Transverse uniformity

The pressure histogram at the time of x-ray exposure can be further broadened by the presence of pressure gradients transverse to the axis of compression. This contribution to the broadening depends in part on the extent of the drive laser illumination compared to the diameter of the pinhole, as well as to the thickness of the window and sample.

For x-rays scattered along the axis of the aperture (exit angle $\beta = 0$), the signal probes an area of the sample equal to the area of the aperture, centered on the axis. For a diffracting sample offset from the pinhole by the thickness of a window layer h_w and as β increases, the region contributing to the diffracted signal will move away from the axis of the aperture. The thickness of the sample h_s will have a similar effect. The distance of the center of the sample region from the axis (the impact parameter), b, is given by

$$b = d_p/2 + (h_w + h_s/2)\tan\beta, \tag{60}$$

where d_p is the diameter of the pinhole. The maximum impact parameter $b_{\max}$ on the sample for which there is any unobstructed ray through the aperture occurs for an exit angle equal to the critical angle of the aperture, $\beta = \beta_{\text{crit}} = \tan^{-1}(d_p/h_p)$,

$$b_{\max} = \frac{d_p}{h_p}\left(\frac{1}{2}h_p + h_w + \frac{1}{2}h_s\right). \tag{61}$$

Note that laser compression of the sample and window will reduce h_w and h_s from their initial values during the x-ray exposure time interval.

Focal-spot conditioning at the NIF, OMEGA, and OMEGA EP optionally includes phase plates to shape the focal–spot profile and improve the illumination uniformity within the spot. The resulting focal spot is an ellipse 1200 μm wide by 900 μm high when projected onto a vertical surface at the NIF and typically an 800 μm or 1100 μm diam circle at OMEGA and OMEGA EP. The aperture and window were designed to approximately match b_{max} with the focal spot; at the NIF, the standard setup uses $d_p = 400$ μm, $h_p = 100$ μm, and $h_w = 100$ μm, giving $b_{max} = 600$ μm. At Omega and OMEGA EP,

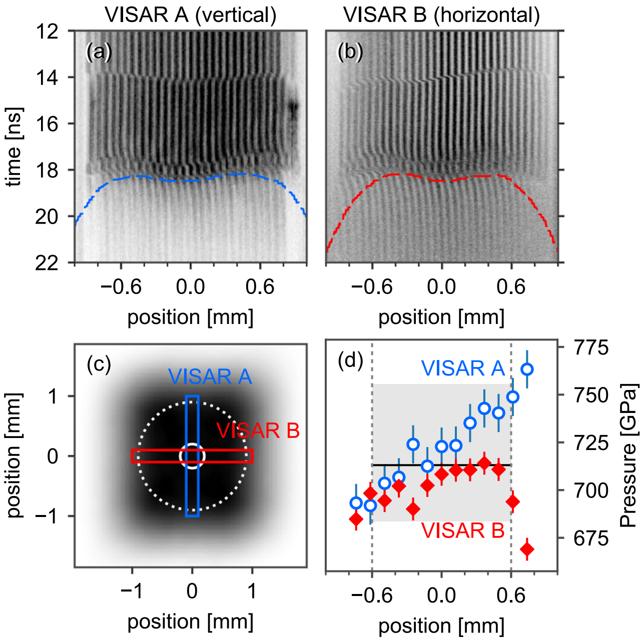

FIG. 23. [(a) and (b)] VISAR records of NIF shot N130919, which used a tiled drive spot and orthogonal imaging directions. The fast camera sweep reveals small temporal variations in the elastic (14 ns) and plastic (18 ns) wave breakouts from the free surface. (c) Calculated laser irradiance on the drive surface, with VISAR fields of view overlayed, and lineouts as dashed lines in subfigures (a) and (b). The solid inner and dashed outer circles indicate the standard 0.4 mm pinhole diameter and the larger 1.8 mm diameter used in this experiment. (d) Pressure analysis as a function of position shows the sample pressure uniformity during x-ray exposure satisfying the ±5% peak-to-valley design goal over the central 1.2 mm width (shaded region).

the standard setup uses $d_p = 300\ \mu$m, $h_p = 75\ \mu$m, and $h_w = 50\ \mu$m, giving $b_{max} = 350\ \mu$m.

For applications where high transverse uniformity is essential, we have also designed a tiled beam-pointing scheme at the NIF. This profile was designed with ray-tracing and radiation-hydrodynamic codes to maintain the transverse illumination and pressure uniformity, respectively, to better than ±5% over a 1.2 mm region (corresponding to $b_{\max} = 600\ \mu$m).

To confirm the uniformity of this design, a dedicated experiment was performed at the NIF, where the aperture diameter was increased to 1.8 mm. The VISAR field of view was expanded to 2 mm, and the two VISAR channels had their imaging directions arranged orthogonal to each other so that one channel imaged in the horizontal direction and the other in the vertical. The results from this experiment are shown in Fig. 23, where a spatially dependent characteristics-analysis of the VISAR record shows 1σ pressure variations of 2.3% over the central 1.2 mm region and satisfying the design goal of ±5% peak-to-valley.

V. CONCLUSIONS

We report the design and performance of a platform to measure the x-ray diffraction pattern from samples dynamically compressed at large laser facilities to high pressures exceeding 1 TPa. The diffraction pattern is recorded over about 1.5π solid angle, with 2θ x-ray scattering angular coverage between 10° and 120°, 1° resolution, and 0.2° precision. Up to two independently timed x-ray sources can be flashed during the sample compression, where x-ray probe wavelength is selectable between 0.8 Å and 1.9 Å.

High-precision velocimetry measurements are used to simultaneously determine the pressure history in the sample, in particular, at the time(s) of x-ray exposure. Pressure uniformity in the sample better than 3% has been demonstrated during the time of x-ray exposure.

The platform has been used (1) to measure the density–pressure equation of state and determine the crystal structure of a variety of materials, including discovery of several new phases; (2) to evaluate the strain-induced texturing or de-texturing after some phase transitions; and (3) to verify solidity and observe liquid phases, thereby examining the melt line at high pressures. Dual x-ray probes unlock new exploration of the kinetics of phase transitions at nanosecond time scales, including hysteresis and the strain-rate dependence of phase boundaries. Manuscripts describing new diffraction results on several materials compressed up to 2 TPa are currently in preparation.

Over the last century, x-ray diffraction has been an invaluable tool for probing and understanding materials, and we are pleased to push this capability toward the current frontier of high-pressure science.

ACKNOWLEDGMENTS

The authors express their profound appreciation for the extensive efforts of the engineering, target fabrication, and facility staff at Lawrence Livermore National Laboratory that made this experimental platform possible. In addition, we express deep gratitude for the helpful insights and useful discussions with S. J. Burns at the University of Rochester and C. Baily, R. C. Cauble, R. B. Ehrlich, W. J. Evans, J. A. Hawreliak, W. W. Hsing, R. L. Kauffman, J. D. Kilkenny, O. L. Landen, B. R. Maddox, J. W. Pastrnak, and D. W. Swift at Lawrence Livermore National Laboratory, among many others.

This work was performed under the auspices of the U.S. Department of Energy by Lawrence Livermore National Laboratory under Contract No. DE-AC52-07NA27344. A portion of this material is based upon work supported by the Department of Energy National Nuclear Security Administration under Award No. DE-NA0003856, the University of Rochester, and the New York State Energy Research and Development Authority. J.S.W. is grateful for support from the U.K. EPSRC under Grant No. EP/J017256/1.

authors expressed herein do not necessarily state or reflect those of the U.S. Government or any agency thereof.

REFERENCES

[1] E. Gregoryanz, O. Degtyareva, M. Somayazulu, R. J. Hemley, and H.-K. Mao, Phys. Rev. Lett. **94**, 185502 (2005).

[2] C. L. Guillaume, E. Gregoryanz, O. Degtyareva, M. I. McMahon, M. Hanfland, S. Evans, M. Guthrie, S. V. Sinogeikin, and H.-K. Mao, Nat. Phys. **7**, 211 (2011).

[3] M. Millot, S. Hamel, J. R. Rygg, P. M. Celliers, G. W. Collins, F. Coppari, D. E. Fratanduono, R. Jeanloz, D. C. Swift, and J. H. Eggert, Nat. Phys. **14**, 297 (2018).

[4] M. Millot, F. Coppari, J. R. Rygg, A. C. Barrios, S. Hamel, D. C. Swift, and J. H. Eggert, Nature **569**, 251 (2019).

[5] Y. Ma, M. Eremets, A. R. Oganov, Y. Xie, I. Trojan, S. Medvedev, A. O. Lyakhov, M. Valle, and V. Prakapenka, Nature **458**, 182 (2009).

[6] M. D. Knudson, M. P. Desjarlais, A. Becker, R. W. Lemke, K. R. Cochrane, M. E. Savage, D. E. Bliss, T. R. Mattsson, and R. Redmer, Science **348**, 1455 (2015).

[7] R. P. Dias and I. F. Silvera, Science **355**, eaal1579 (2017).

[8] P. M. Celliers, M. Millot, S. Brygoo, R. S. McWilliams, D. E. Fratanduono, J. R. Rygg, A. F. Goncharov, P. Loubeyre, J. H. Eggert, J. L. Peterson, N. B. Meezan, S. Le Pape, G. W. Collins, R. Jeanloz, and R. J. Hemley, Science **361**, 677 (2018).

[9] J. B. Neaton and N. W. Ashcroft, Nature **400**, 141 (1999).

[10] C. J. Pickard and R. J. Needs, Nat. Mater. **9**, 624 (2010).

[11] M.-S. Miao and R. Hoffmann, Acc. Chem. Res. **47**, 1311 (2014).

[12] R. F. Smith, J. H. Eggert, R. Jeanloz, T. S. Duffy, D. G. Braun, J. R. Patterson, R. E. Rudd, J. Biener, A. E. Lazicki, A. V. Hamza, J. Wang, T. Braun, L. X. Benedict, P. M. Celliers, and G. W. Collins, Nature **511**, 330 (2014).

[13] R. F. Smith, D. E. Fratanduono, D. G. Braun, T. S. Duffy, J. K. Wicks, P. M. Celliers, S. J. Ali, A. Fernandez-Pañella, R. G. Kraus, D. C. Swift, G. W. Collins, and J. H. Eggert, Nat. Astronomy **2**, 452 (2018).

[14] J. R. Rygg, J. H. Eggert, A. E. Lazicki, F. Coppari, J. A. Hawreliak, D. G. Hicks, R. F. Smith, C. M. Sorce, T. M. Uphaus, B. Yaakobi, and G. W. Collins, Rev. Sci. Instrum. **83**, 113904 (2012).

[15] F. Coppari, R. F. Smith, J. H. Eggert, J. Wang, J. R. Rygg, A. Lazicki, J. A. Hawreliak, G. W. Collins, and T. S. Duffy, Nat. Geosci. **6**, 926 (2013).

[16] A. Lazicki, J. R. Rygg, F. Coppari, R. Smith, D. Fratanduono, R. Kraus, G. Collins, R. Briggs, D. Braun, D. C. Swift, and J. H. Eggert, Phys. Rev. Lett. **115**, 075502 (2015).

[17] J. Wang, F. Coppari, R. F. Smith, J. H. Eggert, A. E. Lazicki, D. E. Fratanduono, J. R. Rygg, T. R. Boehly, G. W. Collins, and T. S. Duffy, Phys. Rev. B **92**, 174114 (2015).

[18] J. Wang, F. Coppari, R. F. Smith, J. H. Eggert, A. E. Lazicki, D. E. Fratanduono, J. R. Rygg, T. R. Boehly, G. W. Collins, and T. S. Duffy, Phys. Rev. B **94**, 104102 (2016).

[19] D. N. Polsin, D. E. Fratanduono, J. R. Rygg, A. Lazicki, R. F. Smith, J. H. Eggert, M. C. Gregor, B. H. Henderson, J. A. Delettrez, R. G. Kraus, P. M. Celliers, F. Coppari, D. C. Swift, C. A. McCoy, C. T. Seagle, J.-P. Davis, S. J. Burns, G. W. Collins, and T. R. Boehly, Phys. Rev. Lett. **119**, 175702 (2017).

[20] J. K. Wicks, R. F. Smith, D. E. Fratanduono, F. Coppari, R. G. Kraus, M. G. Newman, J. R. Rygg, J. H. Eggert, and T. S. Duffy, Sci. Adv. **4**, eaao5864 (2018).

[21] D. N. Polsin, D. E. Fratanduono, J. R. Rygg, A. E. Lazicki, R. F. Smith, J. H. Eggert, M. C. Gregor, B. J. Henderson, X. Gong, J. A. Delettrez, R. G. Kraus, P. M. Celliers, F. Coppari, D. C. Swift, C. A. McCoy, C. T. Seagle, J.-P. Davis, S. J. Burns, G. W. Collins, and T. R. Boehly, Phys. Plasmas **25**, 082709 (2018).

[22] T. R. Boehly, D. L. Brown, R. S. Craxton, R. L. Keck, J. P. Knauer, J. H. Kelly, T. J. Kessler, S. A. Kumpan, S. J. Loucks, S. A. Letzring, F. J. Marshall, R. L. McCrory, S. F. B. Morse, W. Seka, J. M. Soures, and C. P. Verdon, Opt. Commun. **133**, 495 (1997).

[23] D. D. Meyerhofer, J. Bromage, C. Dorrer, J. H. Kelly, B. E. Kruschwitz, S. J. Loucks, R. L. McCrory, S. F. B. Morse, J. F. Myatt, P. M. Nilson, J. Qiao, T. C. Sangster, C. Stoeckl, L. J. Waxer, and J. D. Zuegel, J. Phys.: Conf. Ser. **244**, 032010 (2010).

[24] E. I. Moses, R. N. Boyd, B. A. Remington, C. J. Keane, and R. Al-Ayat, Phys. Plasmas **16**, 041006 (2009).

[25] The hydrodynamic impedance of a material is the product of the mass density and the sound speed.

[26] W. J. Nellis, S. T. Weir, and A. C. Mitchell, Phys. Rev. B **59**, 3434 (1999).

[27] M. F. Ahmed, A. House, R. F. Smith, J. Ayers, Z. S. Lamb, and D. W. Swift, Proc. SPIE **8850**, 88500N (2013).

[28] R. M. Vignes, M. F. Ahmed, J. H. Eggert, A. C. Fisher, D. H. Kalantar, N. D. Masters, C. A. Smith, and R. F. Smith, J. Phys.: Conf. Ser. **717**, 012115 (2016).

[29] P. M. Celliers, D. K. Bradley, G. W. Collins, D. G. Hicks, T. R. Boehly, and W. J. Armstrong, Rev. Sci. Instrum. **75**, 4916 (2004).

[30] R. M. Malone, G. A. Capelle, J. R. Celeste, P. M. Celliers, B. C. Frogget, R. L. Guyton, M. I. Kaufman, T. L. Lee, B. J. MacGowan, E. W. Ng, I. P. Reinbachs, R. B. Robinson, L. G. Seppala, T. W. Tunnell, and P. W. Watts, Proc. SPIE **6342**, 634220 (2007).

[31] P. J. Wegner, J. M. Auerbach, T. A. Biesiada, S. N. Dixit, J. K. Lawson, J. A. Menapace, T. G. Parham, D. W. Swift, P. K. Whitman, and W. H. Williams, Proc. SPIE **5341**, 180–190 (2004).

[32] National Ignition Facility User Guide, Lawrence Livermore National Laboratory, 2016.

[33] M. A. Barrios, S. P. Regan, K. B. Fournier, R. Epstein, R. Smith, A. Lazicki, R. Rygg, D. E. Fratanduono, J. Eggert, H.-S. Park, C. Huntington, D. K. Bradley, O. L. Landen, and G. W. Collins, Rev. Sci. Instrum. **85**, 11D502 (2014).

[34] F. Coppari, R. F. Smith, D. B. Thorn, D. A. Liedahl, R. G. Kraus, A. E. Lazicki, M. Millot, J. R. Rygg, and J. H. Eggert, Rev. Sci. Instrum. **90**, 125113 (2019).

[35] M. A. Barrios, D. A. Liedahl, M. B. Schneider, O. Jones, G. V. Brown, S. P. Regan, K. B. Fournier, A. S. Moore, J. S. Ross, O. Landen, R. L. Kauffman, A. Nikroo, J. Kroll, J. Jaquez, H. Huang, S. B. Hansen, D. A. Callahan, D. E. Hinkel, J. D. Moody, and D. Bradley, Phys. Plasmas **23**, 056307 (2016).

[36] S. F. Khan, P. M. Bell, D. K. Bradley, S. R. Burns, J. R. Celeste, L. S. Dauffy, M. J. Eckart, M. A. Gerhard, C. Hagmann, D. I. Headley, J. P. Holder, N. Izumi, M. C. Jones, J. W. Kellogg, H. Y. Khater, J. R. Kimbrough, A. G. Macphee, Y. P. Opachich, N. E. Palmer, R. B. Petre, J. L. Porter, R. T. Shelton, T. L. Thomas, and J. B. Worden, Proc. SPIE **8505**, 850505 (2012).

[37] B. Yaakobi, D. Steel, E. Thorsos, A. Hauer, B. Perry, S. Skupsky, J. Geiger, C. M. Lee, S. Letzring, J. Rizzo, T. Mukaiyama, E. Lazarus, G. Halpern, H. Deckman, J. Delettrez, J. Soures, and R. McCrory, Phys. Rev. A **19**, 1247 (1979).

[38] D. B. Thorn, F. Coppari, T. Doeppner, M. J. MacDonald, S. P. Regan, and M. B. Schneider, Rev. Sci. Instrum. **89**, 10F119 (2018).

[39] M. Hohenberger, F. Albert, N. E. Palmer, J. J. Lee, T. Döppner, L. Divol, E. L. Dewald, B. Bachmann, A. G. MacPhee, G. LaCaille, D. K. Bradley, and C. Stoeckl, Rev. Sci. Instrum. **85**, 11D501 (2014).

[40] B. R. Maddox, H. S. Park, B. A. Remington, N. Izumi, S. Chen, C. Chen, G. Kimminau, Z. Ali, M. J. Haugh, and Q. Ma, Rev. Sci. Instrum. **82**, 023111 (2011).

[41] M. N. Rosenbluth, Phys. Rev. Lett. **29**, 565 (1972).

[42] C. G. Ryan, E. Clayton, W. L. Griffin, S. H. Sie, and D. R. Cousens, Nucl. Instrum. Methods Phys. Res., Sect. B **34**, 396 (1988).

[43] M. Morháč, J. Kliman, V. Matoušek, M. Veselský, and I. Turzo, Nucl. Instrum. Methods Phys. Res., Sect. A **401**, 113 (1997).

[44] M. Morháč and V. Matoušek, Appl. Spectrosc. **62**, 91 (2008).

[45] D. J. Erskine, J. H. Eggert, P. M. Celliers, and D. G. Hicks, Rev. Sci. Instrum. **87**, 033106 (2016).

[46] J. R. Maw, AIP Conf. Proc. **706**, 1217–1220 (2004).

[47] S. D. Rothman and J. Maw, J. Phys. IV **134**, 745–750 (2006).

[48] S. J. Ali, R. G. Kraus, D. E. Fratanduono, D. C. Swift, and J. H. Eggert, J. Appl. Phys. **121**, 195901 (2017).

[49] P. M. Celliers, G. W. Collins, D. G. Hicks, and J. H. Eggert, J. Appl. Phys. **98**, 113529 (2005).

[50] D. K. Bradley, J. H. Eggert, R. F. Smith, S. T. Prisbrey, D. G. Hicks, D. G. Braun, J. Biener, A. V. Hamza, R. E. Rudd, and G. W. Collins, Phys. Rev. Lett. **102**, 075503 (2009).

[51] D. E. Fratanduono, T. R. Boehly, P. M. Celliers, M. A. Barrios, J. H. Eggert, R. F. Smith, D. G. Hicks, G. W. Collins, and D. D. Meyerhofer, J. Appl. Phys. **110**, 073110 (2011).
[52] D. E. Fratanduono, T. R. Boehly, M. A. Barrios, D. D. Meyerhofer, J. H. Eggert, R. F. Smith, D. G. Hicks, P. M. Celliers, D. G. Braun, and G. W. Collins, J. Appl. Phys. **109**, 123521 (2011).
[53] L. E. Kirsch, S. J. Ali, D. E. Fratanduono, R. G. Kraus, D. G. Braun, A. Fernandez-Pañella, R. F. Smith, J. M. McNaney, and J. H. Eggert, J. Appl. Phys. **125**, 175901 (2019).
[54] M. D. Furnish, L. C. Chhabildas, and W. D. Reinhart, Int. J. Impact Eng. **23**, 261 (1999).
[55] P. A. Rigg, M. D. Knudson, R. J. Scharff, and R. S. Hixson, J. Appl. Phys. **116**, 033515 (2014).
[56] J.-P. Davis, M. D. Knudson, L. Shulenburger, and S. D. Crockett, J. Appl. Phys. **120**, 165901 (2016).
[57] C. T. Seagle, J.-P. Davis, and M. D. Knudson, J. Appl. Phys. **120**, 165902 (2016).
[58] D. E. Fratanduono, J. H. Eggert, M. C. Akin, R. Chau, and N. C. Holmes, J. Appl. Phys. **114**, 043518 (2013).
[59] *International Tables for Crystallography, Volume C: Mathematical, Physical and Chemical Tables*, 1st ed., edited by E. Prince (International Union of Crystallography, Chester, 2006).
[60] A. L. Meadowcroft, C. D. Bentley, and E. N. Stott, Rev. Sci. Instrum. **79**, 113102 (2008).
[61] T. Bonnet, M. Comet, D. Denis-Petit, F. Gobet, F. Hannachi, M. Tarisien, M. Versteegen, and M. M. Aléonard, Rev. Sci. Instrum. **84**, 103510 (2013).
[62] N. Izumi, J. Lee, E. Romano, G. Stone, B. Maddox, T. Ma, V. Rekow, D. K. Bradley, and P. Bell, Proc. SPIE **8850**, 885006 (2013).
[63] G. J. Williams, B. R. Maddox, H. Chen, S. Kojima, and M. Millecchia, Rev. Sci. Instrum. **85**, 11E604 (2014).
[64] P. Beiersdorfer and G. V. Brown, Phys. Rev. A **91**, 032514 (2015).
[65] R. Si, X. L. Guo, K. Wang, S. Li, J. Yan, C. Y. Chen, T. Brage, and Y. M. Zou, Astron. Astrophys. **592**, A141 (2016).
[66] C. Chantler, J. Laming, J. Silver, D. Dietrich, P. Mokler, E. Finch, and S. Rosner, Phys. Rev. A **80**, 022508 (2009).
[67] H. P. Klug, J. Am. Chem. Soc. **68**, 1493 (1946).
[68] The lead sample experiences heating during x-ray exposure by the x-rays from the source, which may increase the temperature by several hundred K. Thermal expansion during this exposure results in a lattice constant a few parts per thousand larger than the ambient value. This effect was mitigated in shot N160518-001 by using a lower laser energy to drive the x-ray source (11 kJ instead of 30–100 kJ). However, this lower x-ray source drive results in a lower temperature in Ge and a red-shifting of the He_α complex also of a few parts per thousand.
[69] D. E. Fratanduono, R. F. Smith, D. G. Braun, J. R. Patterson, R. G. Kraus, T. S. Perry, A. Arsenlis, G. W. Collins, and J. H. Eggert, J. Appl. Phys. **117**, 245903 (2015).